Effects of the Saffman lift force on particle statistics and turbulence modulation in two-phase flow

Jinchi Li [1], Ping Wang [1] and Xiaojing Zheng [2,*]
[1] Key Laboratory of Mechanics on Disaster and Environment in Western China, The Ministry of Education of China, Department of Mechanics, Lanzhou University, Lanzhou 730000, China
[2] Research Center for Applied Mechanics, School of Mechano-Electronic Engineering, Xidian University, Xi'an 710071, China

(Received 21 July 2023; accepted 17 January 2024; published 1 March 2024)

Point-particle direct numerical simulations of horizontal open-channel turbulence two-way coupled with inertial particles ($St^+ = 1, 31, 100$) are performed to investigate the effects of the Saffman force (the shear-induced lift force) on particle motion and turbulence modulation. The friction Reynolds numbers of particle-free wall turbulence are $Re_\tau = 180$ and 580, respectively. The results show that for $St^+ = 31$ and $Re_\tau = 180$, the near-wall negative lift force increases the rebound velocity of particles after particle-wall collisions and prevents them from following the fluid motions. Therefore, the accumulation of the particles near the wall and the preferential concentration in the low-speed streaks are suppressed by the lift force. As a result, the turbulent velocity fluctuations are decreased below the buffer layer. The destruction of the conditional hairpin vortex is observed because particles with the lift force are easy to cross the vortex core. In the outer layer, the particle-turbulence interaction is increased by the lift force because of higher particle concentration. The significance of the lift force on turbulence modulation decreases with the increasing Reynolds number, albeit the near-wall lift force itself becomes more important at high Reynolds number. Finally, even with the shear-induced lift force, the particle-turbulence interaction is still the strongest for the moderate-inertia particle in the St^+ range studied in this paper.

DOI: 10.1103/PhysRevFluids.9.034301

I. INTRODUCTION

The small particles that move in the shear flows are usually subjected to the shear-induced lift force (Saffman force), which causes them to migrate in the flow-normal direction [1,2]. In wall-bounded turbulence, including channel and flat plate boundary layer, the Saffman force is on the order of Refs. [3–6] or even several times higher [7] than the drag force near the wall based on different lift force models (Appendix A). Since the Saffman lift force is proportional to the slip velocity between the particle and the fluid, it will increase particle deposition when particle moves faster than fluid [4,8] and vice versa [9]. Therefore, the Saffman force is one of the key factors for particle transport [10] and hence the interaction among phases in turbulent multiphase flow. This study aims to investigate how the Saffman force affects the statistics and structures of the wall-bounded two-phase turbulence.

Numerical simulation is one of the most common approaches to study particle-turbulence interactions in two-phase flow because it can reveal various phenomena, details, and physical mechanisms under controllable or ideal conditions. In the numerical simulations, the coupling between the

*xjzheng@lzu.edu.cn

particles and turbulence involves two important aspects, namely: whether particles can change the fluid dynamics, and if so, how to feedback. Usually, the strength of two-phase interaction is mainly determined in terms of the particle volume fraction ϕ_v or the mass loading ϕ_m [11]. When ϕ_v and ϕ_m are relatively low, the major influence is that of the turbulence on the dynamics of particles. Under this condition, the one-way coupled simulation is often performed. The feedback of the particles on the turbulent dynamics cannot be ignored when ϕ_v and ϕ_m are large enough, therefore the two-way coupling (the feedback of particles must be involved in the governing equation of turbulence) or even the four-way coupling method (the particle–particle interactions should be involved too) is applied. In the latter two cases, the feedback of the particles on turbulence is either introduced in the framework of the fully resolved simulations in which particles are treated as boundaries of the flow or in the framework of the point-particle model, in which typically important forces need to be included in the Lagrangian equations of particle motion.

In the particle-resolved (PR) method, the total hydrodynamic force acting on the particle can be calculated directly by integrating the hydrodynamic stress tensor over a particle's surface because the flow near the particles is resolved. However, high computational cost and memory consumption are necessary [12,13]. The numerical simulations which can be compared with practical application often need to resolve a huge number of particles. Therefore, PR simulation is difficult to achieve in the foreseeable future in spite of its high accuracy [11]. In the point-particle (PP) simulations, it is recognized that the most important hydrodynamic component in the particle's governing equation is the drag force for heavy particles (density ratio much larger than one) [3,14,15]. Numerous investigations have focused on and revealed the phenomena and mechanisms of two-phase interactions in the wall-bounded turbulence laden with particles only affected by the drag force (hereinafter called inertial particles). For example, the aggregation of inertial particles in the low-speed streaks near the wall of wall-bounded turbulence has been revealed based on the one-way coupled numerical simulations [16–19]. This aggregation is most significant when the inertia of particles is $\mathrm{St}^+ \sim O(10)$. Here, the particle inertia is defined as $\mathrm{St}^+ = \tau_p u_\tau^2/v$, where $\tau_p (= d_p^2 \rho_p / 18 \rho_f v)$ is the particle response time with diameter d_p and density ρ_p, u_τ is the friction velocity of wall turbulence, v and ρ_f are the kinematic viscosity and density of the fluid, respectively. The particles with higher or lower inertia are relatively uniformly distributed. The features of large-scale particle streaks in the buffer layer of wall-bounded turbulence depend on both particle inertia and turbulent Reynolds number [20]. Besides, the particles would migrate along the direction where the intensity of turbulence decreases [21]. The so-called turbophoresis is the most apparent when the response time of the particle matches the local turbulence time near the wall ($\mathrm{St}^+ = 10 \sim 100$), which leads to the highest particle concentration there [19,22,23]. For the same St^+, the deposition rate of particles increases with the Reynolds number Re_τ ($= u_\tau H/v = 150 \sim 1000$, where H is the characteristic length scale of wall-bounded turbulence) [23]. Further, the two-way coupled simulations have revealed that the particles mostly suppress the vertical and spanwise turbulent intensity while the influence of the particles on the streamwise turbulent intensity significantly depends on particle inertia. The argument is especially strong for moderate-inertia particles (typically, $\mathrm{St}^+ = 10 \sim 50$) that aggregate most obviously. Lee and Lee [24] found that the particles decrease the streamwise turbulent fluctuation above the buffer layer at an early stage of two-phase flow evolution, while others reported an enhancement of the streamwise turbulence intensity at a statistically steady state [25–29]. In addition, inertial particles could also affect the shape and energy contribution of turbulent coherent structures such as the hairpin vortices, quasistreamwise vortices, low-speed streaks, and large-scale motions/very-large-scale motions (LSMs/VLSMs) in the inner and outer layer [24,27,30–34]. It was found that moderate-inertia particles [$\mathrm{St}^+ \sim O(10)$] greatly reduce the number of near-wall quasistreamwise vortices [24], increase the spanwise scale of quasistreamwise vortices [30] and lead to longer low-speed streaks [27]. Most recently, Gao *et al.* [35] performed point-particle direct numerical simulations (PP-DNS) in an open channel at $\mathrm{Re}_\tau = 5186$. They found that the particles make the coherent structures become wider and shorter in the spanwise and streamwise directions, respectively. Besides, particles with $\mathrm{St}_k = O(1)$ ($\mathrm{St}^+ = 8.2$–25) are most likely to preferentially concentrate in Q2 events in the turbulent planar Couette flow and weaken the

eddy strength. The influence of particles on the conditional hairpin vortex is more pronounced at high Reynolds number [31]. High-inertia particles ($St^+ = 51.6$) weaken large-scale vortices while low-inertia particles ($St^+ = 4.44$) enhance them in the planar Couette flow, which are similar to the results of channel turbulence [33].

Costa *et al.* [36,37] compared PR-DNS with PP-DNS and found that PP-DNS with only the drag force significantly underestimates near-wall particle velocity fluctuations. The addition of the Saffman force improves the prediction of particle statistics to a certain extent, which depends on the choice of the lift force model. Their results demonstrated that PP-DNS requires at least both the drag force and the Saffman force to match PR-DNS. A variety of different Saffman lift force models have been proposed by theoretical and experimental methods (see Appendix A) and there are a series of studies so far about the qualitative and quantitative effects of the Saffman shear lift force on deposition rate and concentration of particles in the turbulent multiphase flows. However, it is still unknown which is the best model because the lift force model depends in unknown ways on many parameters, such as Reynolds number, Stokes number, distance from the wall, and particle volume fraction [35]. The differences in particle dynamics caused by the lift force were the main concerns in a few studies. McLaughlin [3] investigated the particle transport in a vertical channel by one-way coupled PP-DNS ($Re_\tau = 125$, $St^+ = 2 \sim 6$) using Saffman model. Their results showed that the shear lift force is more significant near the wall where the negative lift forces make particles move more rapidly toward the wall. Zhang and Ahmadi [4] also employed the Saffman model in their one-way coupled PP-DNS and indicated that both the drag force and the shear lift force play dominant roles in the transport and deposition of larger particles in a vertical channel ($Re_\tau = 125$). Marchioli and Soldati [9] performed one-way coupled DNS of two-phase flow in a vertical channel ($Re_\tau = 150$, $St^+ = 3.8 \sim 116.3$) using the Mclaughlin91 model and concluded that particle fluxes to the wall increase a little when the shear lift force is involved and this effect is smaller for high-inertia particle. Arcen *et al.* [7] found that the vertical lift force (CM model) near the wall increases with the increase of particle inertia ($St^+ = 1.2, 6.8, 27.1$) at low Reynolds number $Re_\tau \approx 184$, even up to 6.5 times of the drag force. Later, Marchioli *et al.* [22] adopted the combination of the Saffman model and the Mclaughlin91 model in their simulations and pointed out that the shear lift force increases the drift of particles with $St^+ < 5$ towards the wall and reduces the transport of particles with $St^+ > 25$, which give rise to stronger accumulation of the low-inertia particles near the wall. Barati *et al.* [38] simulated the continuous saltation process of a particle over a particle bed. Their result showed that the saltation height, length, and streamwise velocity of the particle are apparently increased by the shear lift force as compared to the case without lift force. Because the lift force was linked to the drag force through $\boldsymbol{F}_L = 0.7\boldsymbol{F}_D$ in their study, which is a rough and unconventional model, the lift force has a very significant impact on particle motion. Mortimer *et al.* [6] investigated the two-phase turbulent channel flow laden with particles of different inertias ($St^+ = 0.1, 50, 92$) using one-way coupling method and Mei model. They found that for $St^+ = 0.1$, the maximum ratio of lift force to drag force is around 45% in the buffer layer. However, the maximum ratio is only around 30% for $St^+ = 50$ and 92. Recently, Rousta *et al.* [39] preformed one-way coupled PP-DNS ($Re_\tau = 180$, $St^+ = 1 \sim 130$) using Mclaughlin91 model in a vertical turbulent channel flow. They compared the deposition velocities of particles with the existing experimental and numerical results and found that when the Saffman lift force is included, good agreement between their results and experimental measurements can be obtained.

As particle volume fraction (or mass loading) increases, two-way coupling becomes important. In the two-way coupling framework, the lift force not only affects the particle transport as compared to the one-way coupling case but also influences turbulence modulation. Nasr *et al.* [40] simulated the two-way coupled horizontal channel turbulence ($Re_\tau = 150$, $St^+ = 14, 20$) using the Mclaughlin93 model and revealed that two-way coupling weakened the preferential distribution of particles compared with one-way coupling. A few two-way coupled numerical studies were conducted to further investigate the turbulence modulation by particles with lift force. However, they did not individually identify the effects of lift force on the modulation. For example, Nasr *et al.* [40] also found that particles with $St^+ = 20$ suppress the turbulence intensity in all directions. The level of

suppression increases with mass loading. In addition to the drag force, the study of Li *et al.* [32] involved both the shear lift force (Mei model) and the rotation lift force in the particle equation. Their results revealed that the presence of particles with $St^+ = 1.8$ and 9 (estimated by $d_p^+ = 0.1472$ and 0.329) suppresses the vertical and spanwise turbulence intensity, while enhances and reduces the streamwise fluid velocity fluctuation near the wall and in the outer layer respectively. The mean spacing of the near-wall streamwise streaks is increased by moderate-inertia particles but reduced by low-inertia particles. Mortimer and Fairweather [41] performed two-way coupled simulations of two-phase flow laden with particles that governed by the drag force, the shear lift force (Mei model), the added mass force, and the pressure gradient force. They found that the particles with $St^+ = 0.1$ enhance the near-wall streamwise turbulent fluctuation, but the particles with $St^+ = 50$ and 92 reduce the near-wall streamwise turbulent fluctuation and enhance them in the logarithmic layer. All three particles suppress the vertical and spanwise turbulence intensity, which is similar to Li *et al.* [32].

According to the above summary, particle dynamics and turbulence modulation by particles governed by shear lift force are still not completely understood though their significance has already been realized. Under what conditions the shear lift force is important and how do the particles acted by the shear lift force influence the two-phase flow are the two main questions to be answered. To this end, we perform DNSs of horizontal open-channel turbulence laden with particles of various inertias ($St^+ = 1, 31, 100$) at two friction Reynolds numbers ($Re_\tau = 180, 580$). The effects of coupling manner between phases are discussed as well. The paper is organized as follows. Numerical procedures are introduced and validated in Sec. II. Then, we present the simulation results of the particles and the turbulence (statistics and coherent structures), which is followed by discussions about the modulation mechanisms in Sec. III. In this section, the effects of shear lift force as a function of particle inertia and turbulent Reynolds number are also presented. Finally, the main conclusions are given in section Sec. IV.

II. NUMERICAL PROCEDURES

A. Turbulent channel flow

The incompressible turbulence is governed by the Navier–Stokes equations and continuity equation,

$$\frac{\partial u_i}{\partial t} + \frac{\partial (u_i u_j)}{\partial x_j} = -\frac{\partial p}{\rho \partial x_i} + \nu \frac{\partial^2 u_i}{\partial x_j \partial x_j} + \frac{1}{\rho} f_i, \tag{1}$$

$$\frac{\partial u_i}{\partial x_i} = 0. \tag{2}$$

Here, t is time, ρ, p, and ν are density, pressure, and fluid kinematic viscosity, respectively. u_i represents the fluid velocity component in the streamwise (x), wall-normal (y), and spanwise (z) direction when $i = 1$, 2, and 3, respectively. f_i represents the feedback force of particles to the fluid in two-way coupled simulations.

Figure 1 shows the schematics of the horizontal open-channel flow and the computational periodic cell. The periodic conditions are employed in the horizontal (x, z) directions. The free-slip and no-slip conditions are applied on the upper surface and lower wall, respectively. The computational domain (L_x, L_y, L_z) is set to be ($8\pi H, H, 3\pi H$) (where H represents the half channel height). In single-phase flow, the friction Reynolds numbers based on the wall friction velocity u_τ are $Re_\tau = u_\tau H/\nu = 180, 580$. For the case $Re_\tau = 180$, the mesh is (1024,96,512) and the corresponding grid spacings are $\Delta x^+ = 4.42$, $\Delta y^+ = 0.14 - 4.0$ and $\Delta z^+ = 3.31$, where superscript "+" is the distance based on the wall unit of ν/u_τ. For the case $Re_\tau = 580$, the mesh is (1024,240,1024) and the corresponding grid spacings are $\Delta x^+ = 14.2$, $\Delta y^+ = 0.55$–5.3 and $\Delta z^+ = 5.3$, which is close to the resolution of Wang and Richter [34]. The time step of turbulence simulation is $\Delta t^+ = \Delta t u_\tau^2/\nu = 0.08$ and 0.04 for the two Reynolds numbers respectively to ensure CFL <0.5.

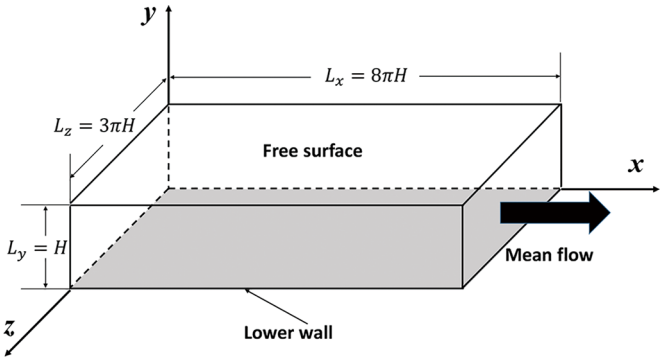

FIG. 1. Schematics of the channel flow and the computational periodic cell.

The governing equations (1) and (2) are numerically solved using the fractional step method with the implicit velocity decoupling procedure [42]. All spatial derivative terms are approximated by a second-order central difference scheme on a staggered grid. On the basis of a block LU decomposition, the velocity-pressure decoupling is achieved through approximate factorization [43,44]. The equations are advanced in time by the Crank–Nicholson scheme. The mean flow driven by a streamwise pressure gradient is adjusted dynamically in time to maintain a constant mass flux [45,46]. Validations of the model can be seen in Appendix B.

B. Lagrangian particle

We simulate moderately dilute suspensions with weak interphase coupling in wall-bounded particle-laden flows [26,41] and the bulk particle volume fraction ϕ_v is set to 1.19×10^{-4}. Several important parameters and methods for numerical simulations are shown in Table I. Similar to other PP-DNSs [20,27,41,46–48], the small spherical particles (sub-Kolmogorov size) are simplified by point-force approximation. Since the particle-to-fluid density ratio is very high ($\rho_p/\rho \gg 1$) and the particle diameter is smaller than the Kolmogorov length scale, the other forces such as the added-mass force, the fluid acceleration force, the Basset history force and the Magnus force on the particles can be ignored [3,7,14,15]. Meanwhile, we assume a high particle Froude number ($Fr_p = u_\tau/(\tau_p g) \gg 1$) to ignore gravity. This is the case, typically, for dust and snow in the air. Only the drag force $\boldsymbol{F}_D$ and the Saffman lift force $\boldsymbol{F}_L$ are considered to emphasize the effect of $\boldsymbol{F}_L$.

TABLE I. Summary of different particle types used in simulation cases A–I.

Case	Re_τ	ρ_p/ρ_f	St^+	N_P	Coupling method	Lift force
A	180	1550	31	1.45×10^6	One	Yes
B	180	1550	31	1.45×10^6	Two	Yes
C	180	1550	31	1.45×10^6	Two	No
D	180	50	1	1.45×10^6	Two	Yes
E	180	50	1	1.45×10^6	Two	No
F	180	5000	100	1.45×10^6	Two	Yes
G	180	5000	100	1.45×10^6	Two	No
H	580	1550	31	4.85×10^7	Two	Yes
I	580	1550	31	4.85×10^7	Two	No

The motion equation of an individual particle can be written as

$$\frac{d^2x_{pi}}{dt^2} = \frac{du_{pi}}{dt} = \frac{F_{Di}}{m_p} + \frac{F_{Li}}{m_p} = \frac{\left(1 + 0.15\mathrm{Re}_p^{0.687}\right)}{m_p\tau_p}(\tilde{u}_i - u_{pi}) + \frac{F_{Li}}{m_p}. \tag{3}$$

where x_{pi} and u_{pi} represent the position and velocity of the particle, respectively. The particle Reynolds number is defined as $\mathrm{Re}_p = |\tilde{\boldsymbol{u}} - \boldsymbol{u}_p|d_p/\nu$, where $|\tilde{\boldsymbol{u}} - \boldsymbol{u}_p|$ represents the modulus of the difference between the fluid velocity vector $\tilde{\boldsymbol{u}}$ and the particle velocity vector $\boldsymbol{u}_p$, called the slip velocity. According to the particle motion equation proposed by Maxey and Riley [49], a key problem is that the slip velocity should be calculated using the undisturbed fluid velocity. However, in two-way coupled simulations, the fluid velocity and velocity gradients are interpolated from a modulated flow field to the particle position since the undisturbed flow field is difficult to obtain [50]. Gualtieri *et al.* [51], Horwitz and Mani [52], and Balachandar *et al.* [53] recently proposed the correction schemes for calculating the approximate undisturbed fluid velocity from the modulated flow field. In the simulations which run for a particle settling under gravity, the first two correction schemes agree better with the analytical solution than the uncorrected one [51,52,54]. The correction proposed by Horwitz and Mani [52] is even closer to the results of PR-DNS in the decaying isotropic turbulent particle-laden flow [55]. Recently, the Gualtieri correction [51] was employed to simulate two-phase wall turbulence and investigate turbulence modulation [12,51,56]. To estimate the impact of particle self-induced disturbance, the instantaneous undisturbed velocity is estimated based on Gualtieri's correction (i.e., $\tilde{\boldsymbol{u}} + d_p^2\nabla^2\tilde{\boldsymbol{u}}/24$) for case B (see Table I). It is found that the error between undisturbed and disturbed velocity is less than 1% on average near the wall and decreases with the increase of the wall-normal height. We believe that the particle self-induced disturbance may not have a significant influence on particle motion and turbulence modulation. In addition, Horwitz and Mani [52] pointed out that the trilinear interpolation is more accurate for a particle settling in an otherwise quiescent fluid than higher-order interpolation. Therefore, the undisturbed velocity is not considered in this paper and the trilinear interpolation is deployed to obtain $\tilde{\boldsymbol{u}}$. The existing expressions of the lift force are listed in Appendix A. The Saffman lift force is employed in the simulations. The effects of the lift force models are also simply discussed in Appendix A and no qualitative influences are found. Besides, we performed DNS for moderate-inertia particles with interparticle collisions using a deterministic collision model. It is found that the collisions don't fundamentally alter the influence of lift force on particle behaviors and turbulence modulation at the volume fraction studied (not shown here). Therefore, we opted to neglect the particle-particle collisions.

The particles are uniformly and randomly distributed into the flow field with zero slip velocity after the single-phase turbulence is fully developed. The periodic conditions are applied in the streamwise and spanwise directions for particle motion, namely, the particles that move out of the upper and lower boundaries satisfy the following equations:

$$u_{p2}^* = -u_{p2}, x_{p2}^* = 2H - d_p - x_{p2}(x_{p2} > H - 0.5d_p, u_{p2} > 0), \tag{4}$$

$$u_{p2}^* = -u_{p2}, x_{p2}^* = d_p - x_{p2}(x_{p2} < 0.5d_p, u_{p2} < 0), \tag{5}$$

where u_{p2} and x_{p2} represent the wall-normal velocity and position of the particle touching the boundary, u_{p2}^* and x_{p2}^* represent the wall-normal velocity and position of the particle just after the interaction between the particle and the boundaries.

Time advancement for particle motion equation is performed using the fourth-order Runge–Kutta scheme. The *a posteriori* result shows that the CFL number of particle [$\mathrm{CFL}_P = \max(u_{pi}\Delta t_p/\Delta x_i)$] defined by particle velocity, particle time step ($\Delta t_p^+ = \Delta t_f^+$) and fluid grid is less than 0.5. Similar to previous PP-DNSs [26,46–48], we adopt the particle-source-in cell (PSI-CELL) method [57] in the two-way coupled simulations to collect the feedback force, that is, the drag forces and the shear

lift forces from particles within a given cell volume are summed to give the body force in Eq. (1):

$$f_i = -\frac{1}{V_{\text{cell}}} \sum_{n=1}^{N_{\text{cell}}} (F_{Di} + F_{Li}) \Big|_n , \tag{6}$$

where $(F_{Di} + F_{Li})|_n$ is the force on the nth particle. V_{cell} represents the volume of a fluid cell and N_{cell} represents the number of particles in V_{cell}. Though the feedback force exhibits grid dependency when the number of particles per cell is insufficient using the PSI-CELL method, we opted to proceed with this method. In our simulations, the relative importance of lift force by the PSI-CELL method is close to those by a simplified ERPP method (refer to Appendix C). The particle diameter is $d_p^+ = d_p u_\tau / \nu = 0.6$ in wall units, and $d_{p,K} = 0.38$ and 0.41 when dimensionalized by Kolmogorov length scale within the first off-wall grid at $\text{Re}_\tau = 180$ and 580, respectively.

The simulations last for $T^+ = T u_\tau^2 / \nu = 20\,000$. The statistics of particle and turbulence are performed during $T^+ = 15\,000$–$20\,000$ after the particle-laden flows have achieved the statistically steady state, that is, the Shannon entropy hardly changes with time [19,23,58]. Validations of the model can be seen in Appendix B.

III. RESULTS AND DISCUSSIONS

Previous results for inertial particles revealed that moderate-inertia particles ($\text{St}^+ = 10 \sim 50$) have the strongest accumulation near the wall, the most significant preferential concentration and the strongest modulation on the fluid [19,23,24,59]. The discussions in this section will be centered on the case with $\text{St}^+ = 31$ and $\text{Re}_\tau = 180$. Simulations with other Reynolds numbers and Stokes numbers are mentioned and discussed when necessary.

A. Simulation results

Figure 2 exhibits the instantaneous snapshots of the vortex structures identified as the isosurfaces of the absolute value of λ_{ci}^+ ($= \lambda_{ci} \nu / u_\tau^2$, where λ_{ci} is the imaginary part of the complex eigenvalue of $\nabla \boldsymbol{u}_f$ and $\nabla \boldsymbol{u}_f$ is the fluid velocity gradient tensor [60]), together with the instantaneous particle distribution indicated by small black spheres for one-way coupled simulation with the lift force and two-way coupled simulations with and without the lift force. The isosurface of $\lambda_{ci}^+ = 0.01$ is colored by the wall-normal height. The right panels show λ_{ci}^+ in horizontal plane at $y^+ = 15$ to highlight its near-wall distribution. As can be seen from Fig. 2, the turbulent regions are vividly populated by hairpin vortices and quasistreamwise vortices in all three cases. However, these structures are different in height and quantity due to the difference in particle distribution. When the Saffman lift force is involved in the particle motion equation, the blank area near the wall is larger in the two-way coupled simulation (see Fig. 2(b) and Ref. [61]) than that in the one-way coupled simulation (see Fig. 2(a) and Ref. [61]). The ratio of area with $\lambda_{ci}^+ > 0.01$ to area with $\lambda_{ci}^+ < 0.01$ is 1.08 in two-way coupling case, while that in one-way coupling case is 1.69. The difference in particle distribution between the two cases is not visibly seen since it is the most obvious within the viscous sublayer (will be shown later). However, this difference in particle distribution is remarkable when comparing Figs. 2(b) and 2(c). For these two-way coupled simulations, inertial particles without the Saffman force acting on them accumulate more easily on the wall, giving rise to fewer particles and denser vortex structures in the buffer layer (the ratio of area with $\lambda_{ci}^+ > 0.01$ to area with $\lambda_{ci}^+ < 0.01$ is 1.75).

B. Particle statistics

Figure 3(a) shows the wall-normal profiles of the mean particle concentration ϕ_{vp}, nondimensionalized in terms of the bulk concentration ϕ_v for cases A–C. In particular, ϕ_{vp} is obtained using the uniform grids ($\Delta y_p = 2 d_p$) in the wall-normal direction, which is different from the fluid grid. Note that particles are initially released into the entire computational domain and gradually accumulate

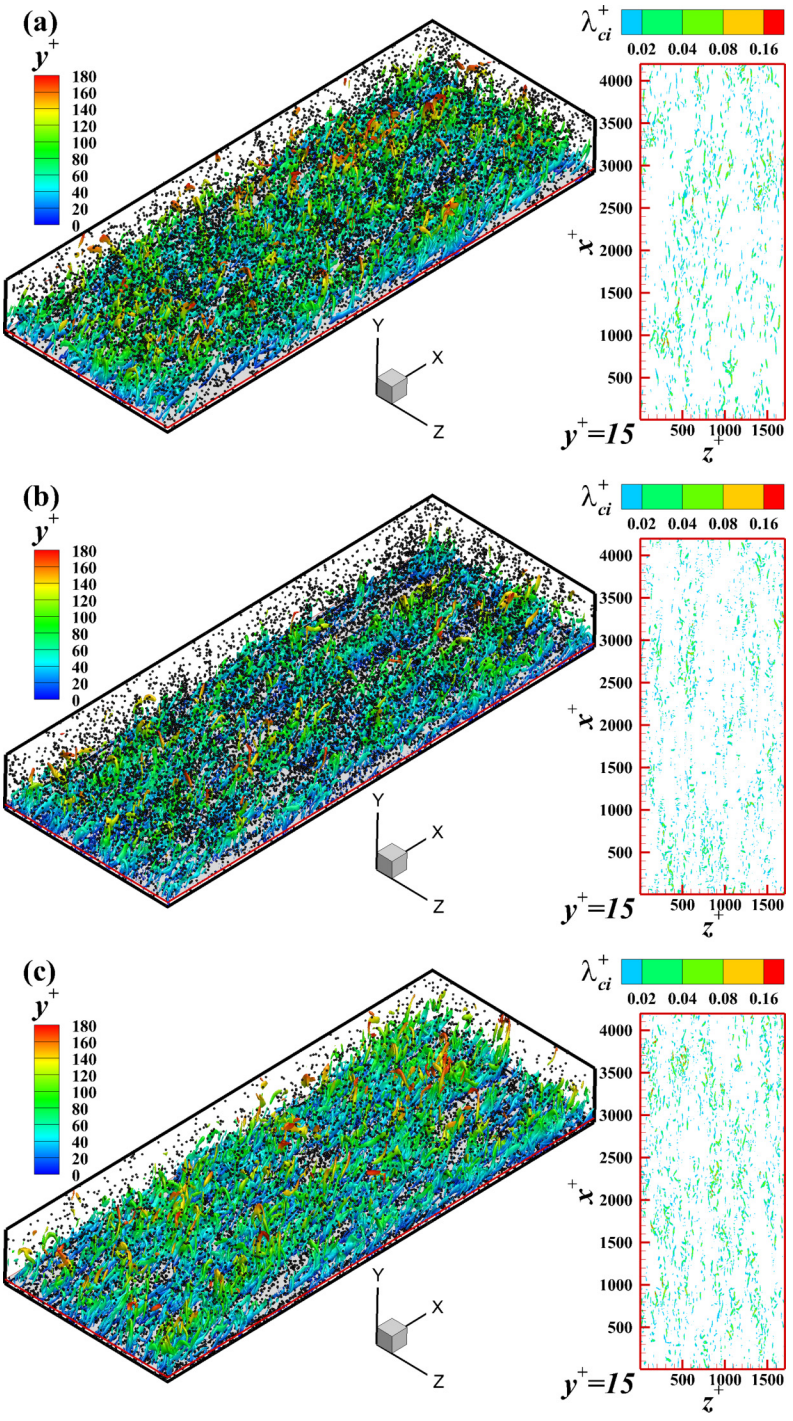

FIG. 2. Instantaneous snapshot of the three-dimensional vortex structures (isosurface for $\lambda_{ci}^+ = 0.01$) in the turbulent region with the particles and λ_{ci}^+ in horizontal plane at $y^+ = 15$ for (a) one-way coupled simulation with Saffman shear lift force, (b) two-way coupled simulation with lift force, and (c) without lift force. The vortex structures are colored by wall-normal height and the particles are indicated by small black spheres ($\mathrm{Re}_\tau = 180$).

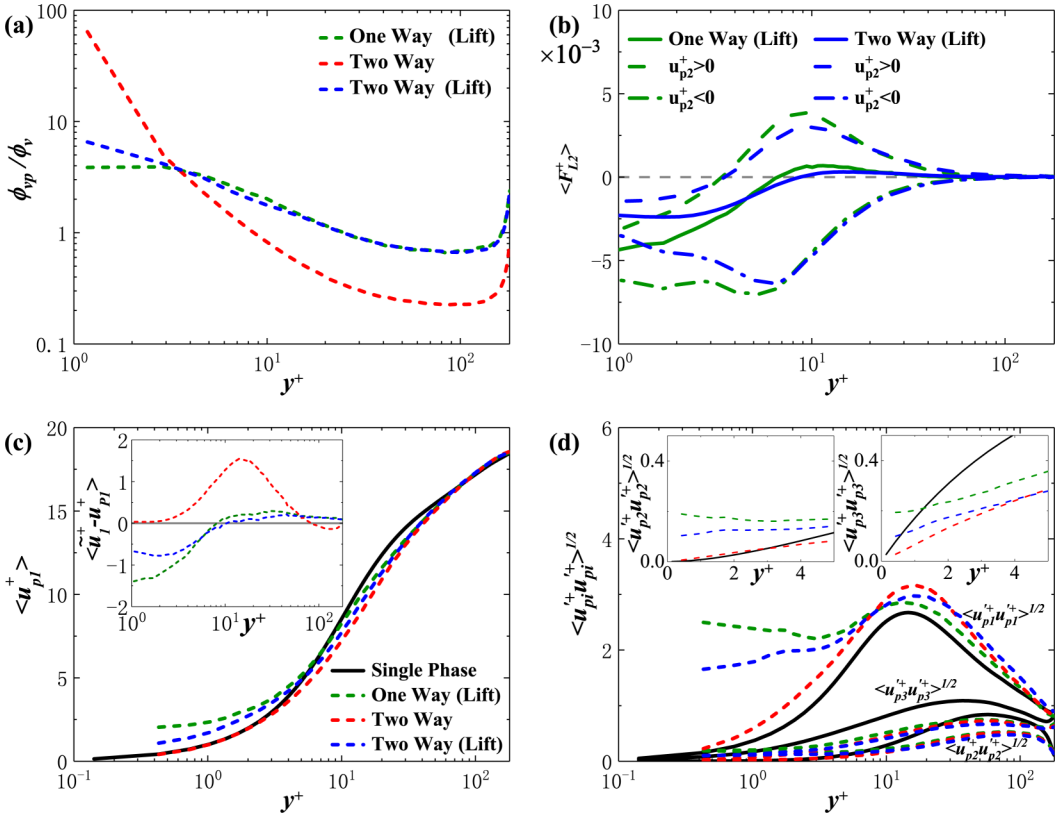

FIG. 3. Particle statistics: (a) particle concentration, (b) mean wall-normal lift force, (c) mean streamwise particle velocity, and (d) RMS particle velocity fluctuations profiles for cases A–C ($\mathrm{Re}_\tau = 180$).

near the wall due to turbophoresis [21] as time goes by. We draw the conclusions based on Fig. 3(a) that particles accumulate more significantly near the wall in two-way coupled simulation than that in one-way coupled simulation and the inertial particles accumulate more significantly than those with the Saffman force [61]. This is apparent since the particle concentration within the first off-wall grid satisfies $\phi_{vp,1,C} > \phi_{vp,1,B} > \phi_{vp,1,A}$. For case C, $\phi_{vp,1,C} = 7.6\times10^{-3}$, which is even one to two orders of magnitude higher than the bulk particle concentration $\phi_v (= 1.19\times10^{-4})$. This phenomenon is consistent with what was reported in Wang *et al.* [59]. As a result, the particle concentration at $y^+ > 60$ is the lowest in this case [also see Fig. 2(c)]. With the lift force in case B, $\phi_{vp,1,B} = 7.78\times10^{-4}$, which is only 1/10 that of case C, indicating that the lift force makes the particle distribution more uniform in wall-normal direction. Therefore, the Saffman force counteracts the turbophoresis effect. It is worth noting that particle concentration in two-way coupled simulation with the lift force decreases monotonically with height, while that in one-way coupled simulation remains essentially constant in the viscous sublayer ($y^+ < 3$). The main difference in particle concentration between one-way and two-way coupled cases seems to be limited to several grids in the vicinity of the wall in our simulations. Note that the peak in the concentration at the open boundary is the result of the free-slip boundary conditions and positive turbophoresis velocity there, which has already been reported in several studies [35,59].

Due to the strong near-wall mean shear $d\langle u\rangle/dy$ ("$\langle\rangle$" represents the ensemble-averaged operation) in wall turbulence [18,62] and the large streamwise slip velocity $\tilde{u}_1 - u_{p1}$, the wall-normal component of the Saffman force must be greater than those in the other two directions according to Saffman model. We therefore just illustrate the wall-normal lift force profiles for cases A and B in

Fig. 3(b). Regardless of the coupling method, both simulations indicate negative mean wall-normal lift force in the region of $y^+ < 7 \sim 8$, which is consistent with McLaughlin [3] and Rousta *et al.* [39], and a slight positive mean wall-normal lift force above (see the solid lines). Most importantly, the lift force on the descending particles ($u_{p2}^+ < 0$) is always negative, while that for ascending particles ($u_{p2}^+ > 0$) is negative very close to the wall and changes to be positive at $y^+ > 3$. This is a very interesting phenomenon which means that once the particles can escape the trapping effect of the wall, they will further move away from the wall under the action of the positive lift force.

Figure 3(c) shows the profiles of the mean streamwise particle velocity for cases A–C. The fluid velocity profile for the single-phase turbulence is also included as a reference. It can be observed that inertial particles (case C, the red dash line) move the most slowly. The hysteresis of particles in the buffer layer is partly due to their preferential distribution in low-speed fluid regions shown later. With the Saffman lift force, more particles are brought toward the wall and move faster than the fluid in the viscous sublayer [39], regardless of the coupling manners. As compared with one-way coupled simulation, the particle velocity in the two-way coupled simulation is apparently lower, especially near the wall. This also results in a small slip velocity $\tilde{u}_1 - u_{p1}$ for the latter case shown in the inset. In the outer layer, the difference among the three cases becomes indistinctive since the lift force becomes negligible [see Fig. 3(b)]. Analogously, we show the RMS particle velocities $\langle u_{pi}'^+ u_{pi}'^+ \rangle^{1/2}$ ($(u_{pi}'^+ = u_{pi}^+ - \langle u_{pi}^+ \rangle)$ for cases A–C (dotted lines) in Fig. 3(d), together with the RMS fluid velocities $\langle u_p'^+ u_p'^+ \rangle^{1/2}$ in the single-phase flow (solid line). The RMS particle velocities are higher than the RMS fluid velocities in the streamwise direction and lower in the spanwise and vertical direction, except for the regions very close to the wall where the particle-wall collisions are relatively frequent [see insets of Fig. 3(d)]. The inertial particles in case C have the lowest RMS velocity near the wall because where the lift force is crucial, particles fall and rebound more quickly. Compared with the two-way coupling case, the RMS velocity of particle is larger in the one-way coupling case due to the higher lift force [see Fig. 3(b)]. In the outer layer, the RMS velocity of particle is similar in all three cases due to the negligible lift force.

The particle numbers in the high-speed region ($u_1'^+ > 0$) and the low-speed region ($u_1'^+ < 0$) are straightforwardly counted. The ratios of $\phi_{vp}(u_1'^+ > 0)$ to $\phi_{vp}(u_1'^+ < 0)$ for cases A–C are shown in Fig. 4(a). $\phi_{vp}(u_1'^+ > 0)/\phi_{vp}(u_1'^+ < 0) > 1$ means a high-speed-region distribution of particles and vice versa. It is clear that more particles collect in the low-speed streaks in the inner layer, while in the outer layer, more particles collect in the high-speed region, regardless of the lift force and coupling manners. This conclusion is consistent with previous PP-DNSs for similar particle inertia [9,23,24,27,34,63]. The differences among various simulations still exist, however. The inertial particles in case C depict the strongest preferential distribution in both inner and outer regions while the Saffman force tends to partially counteract the preferential distribution in the inner layer [61]. Previous studies suggested that entrainment process of particles by coherent wall structures causes the formation of particle preferential concentration in the low-speed regions near the wall [9,18]. The lift force enhances the particle-wall collisions and inhibits the entrainment process of particles, resulting in the weakening of particle preferential concentration. Compared with the two-way coupled simulation, the particles in the one-way coupled case are more uniformly distributed in the flow field within $6 < y^+ < 30$ while more easily clustering in the low-speed regions at $y^+ < 6$. This phenomenon may be due to the positive or negative slip velocity varying with height [see Fig. 3(c)].

Figure 4(b) shows the mean streamwise vorticity magnitude $\langle |\omega_1^+| \rangle$ of the fluid (solid lines) and the vorticity magnitude $\langle |\omega_1^+(u_{p2}^+ > 0)| \rangle$ conditionally averaged at the position of ascending particles ($u_{p2}^+ > 0$) for cases A–C. Without the lift force, the conditionally averaged vorticity $\langle |\omega_1^+(u_{p2}^+ > 0)| \rangle$ is smaller than $\langle |\omega_1^+| \rangle$ within the most of two-phase region, indicating a low-vorticity-region accumulation of the particles. This low-speed and low-vorticity accumulation of inertial particles was also reported before [64]. While with the lift force, $\langle |\omega_1^+(u_{p2}^+ > 0)| \rangle$ is almost the same as $\langle |\omega_1^+| \rangle$ in the viscosity sublayer but smaller than that above. Away from the wall, particle preferential distribution in low-vorticity regions is less clear in all cases. Since the vertical lift force

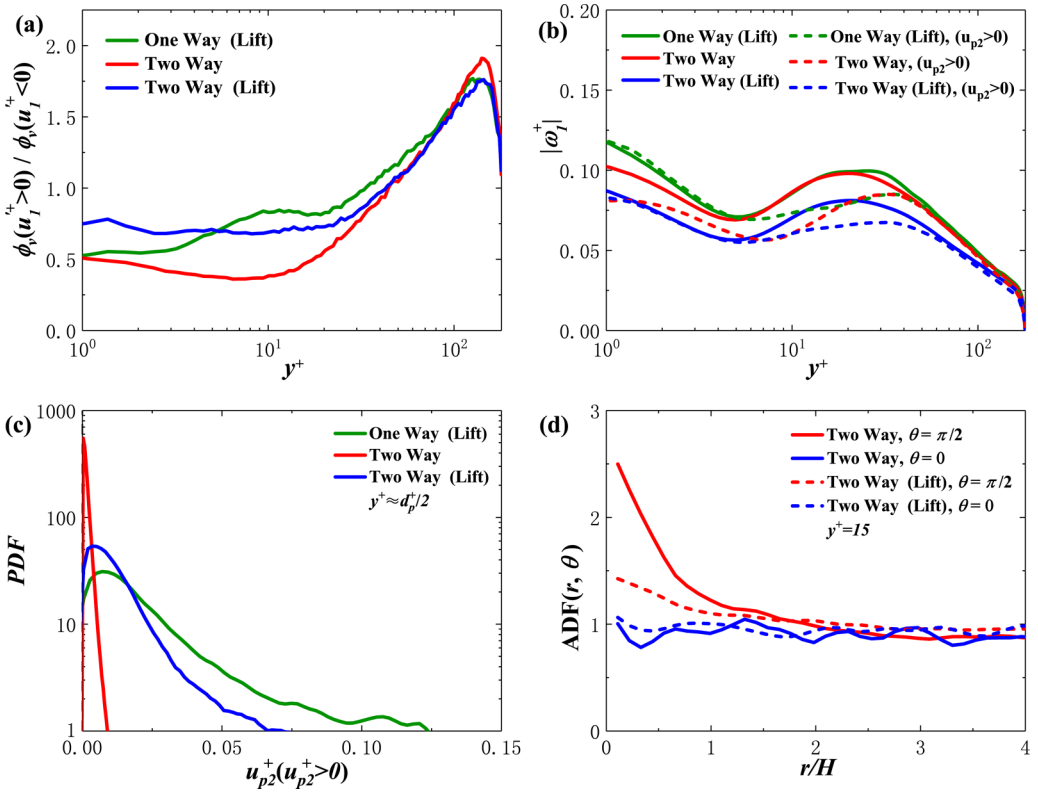

FIG. 4. (a) The ratio between particle concentrations in high-speed fluid ($u_1'^+ > 0$) and low-speed fluid ($u_1'^+ < 0$). (b) The mean streamwise vorticity magnitude $\langle|\omega_1'^+|\rangle$ of the fluid (solid lines) and the absolute vorticity $\langle|\omega_1'^+(u_{p2}^+ > 0)|\rangle$ conditionally averaged at the position of ascending particles ($u_{p2}^+ > 0$). (c) The probability density functions of positive u_{p2}^+ at $y^+ = d_p^+/2$. (d) The angular distribution functions of particles in the x–z slabs with thickness of $\Delta y^+ = 2.0$ in the streamwise and spanwise directions at $y^+ = 15$ ($\mathrm{Re}_\tau = 180$).

is proportional to the streamwise vorticity in magnitude, the high vorticity in the viscosity sublayer results in the high lift force and, consequently, the high impact and rebound velocity as shown in Fig. 4(c) which presents the probability density functions (PDFs) of positive u_{p2}^+ at $y^+ = d_p^+/2$. Therefore, particle behavior there is more significantly governed by the particle-wall interaction. In addition, the PDFs in Fig. 4(c) also suggest a higher positive u_{p2}^+ for one-way coupled simulation (case A) due to the higher lift force in the vicinity of the wall.

Gao *et al.* [35] investigated the anisotropic clustering of particles according to the angular distribution functions (ADFs). In this study, the same method is used to reveal the effect of the lift force on the clustering of particles in the buffer layer. The two-dimensional angular distribution function ADF(r, θ) is defined as

$$\mathrm{ADF}(r,\theta) = \frac{\sum_{i=1}^{n_p} \delta N_i(r,\theta)/(\delta r \delta\theta r n_p)}{N/(L_x L_y)}, \tag{7}$$

where $\delta N_i(r,\theta)$ represents the number of particles which are collected from a sector with thickness of $\Delta y^+ = 2.0$ between $r - \delta r/2$ and $r + \delta r/2$ in the radial direction and $\theta - \delta\theta/2$ and $\theta + \delta\theta/2$ in the angular direction from the center of the ith particle. n_p represents the total number of the central particle from multiple snapshots in time. $N/(L_x L_y)$ represents the randomly distributed particle number density in the sampling height. Here we set $\delta r = 0.2H$ and $\delta\theta = 0.025\pi$ and show the profiles of ADF(r, θ) at $y^+ = 15$ in Fig. 4(d). $\theta = 0$ and $\theta = \pi/2$ represent spanwise and

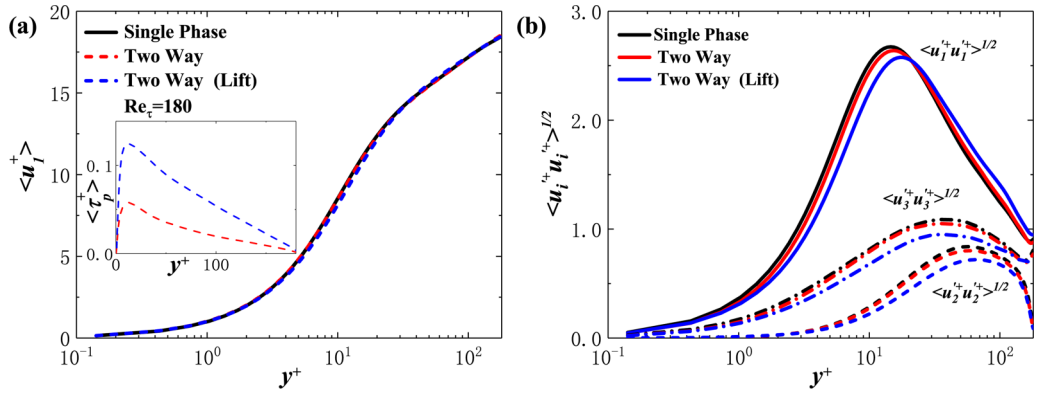

FIG. 5. Turbulence statistics: (a) mean streamwise fluid velocity and (b) RMS fluid velocity fluctuations profiles for cases B and C ($\mathrm{Re}_\tau = 180$). The inset in (a) represents the particle-induced stress.

streamwise directions respectively. For case C, the streamwise ADF(r, θ) near the reference particle is higher than that in the spanwise direction, meaning the anisotropy of particle concentration. However, the Saffman force suppresses the anisotropic clustering of the particles and makes the particle distribution more uniform in the horizontal plane within the buffer layer.

C. Turbulence statistics

Figure 5 illustrates the profiles of turbulence statistics for cases B and C. The presence of particles reduces the mean fluid velocity in the buffer layer due to positive slip velocity and increases $\langle u_1^+ \rangle$ in the outer layer due to constant mass flux. However, since the particle mass loading ($\phi_m = 0.18$) in the simulations is relatively small, the effect of the particles on the mean streamwise velocity of the fluid is almost negligible, except for that in the buffer layer [see Fig. 5(a)]. The inset of the Fig. 5(a) further shows the particle-induced stress τ_p^+ [12,46,65] to investigate the exchange of momentum between the two phases, which is defined by $\tau_p^+ = \int_{H^+}^{y^+} \langle f_1^+(y'^+) \rangle dy'^+$. At steady state, τ_p^+ at the wall (the integral of f_1^+ from the wall to channel center, that is, the entire domain) is zero for cases with or without the lift force, which means that there is no net exchange of momentum between the two phases. However, a larger peak of τ_p^+ occurs in the buffer layer with the lift force, resulting in a more pronounced decrease in mean fluid velocity. Nevertheless, the turbulent velocity fluctuations are visibly affected by the particles, as can be observed in Fig. 5(b). The inertial particles slightly decrease the fluid streamwise velocity fluctuation $\langle u_1'^+ u_1'^+ \rangle^{1/2}$ in the viscous sublayer and increase it above the buffer layer, while that in both wall-normal and spanwise directions is suppressed mildly. The results are consistent with previous PP-DNSs of two-phase turbulence laden with inertial particles [26,28–30,48]. In the inner layer, changes in turbulence intensity are attributed to the suppressed small-scale vortices near the wall [24] and the stronger turbulent low-speed streaks because the particles accumulated in them carry more low-momentum fluid from the near-wall region [66]. The former leads to the weakening of turbulence intensity in the viscous sublayer while the latter enhances the streamwise velocity fluctuations above the buffer layer. We emphasize that the turbulence modulations in the second-order statistics are more pronounced when the lift force is involved. Quantitatively, the maximum difference in $\langle u_1'^+ u_1'^+ \rangle^{1/2}$ with and without the lift force is about 13% at the near-wall peak. However, in consideration of the huge differences in the profiles of particle concentration for the two cases shown in Fig. 2(a), it is interesting that in case B, the lower particle concentration near the wall with lift force results in a more pronounced modulation compared to case C. The differences in turbulence modulations cannot be directly related to the near-wall accumulation of particles. However, in the outer layer, the lift force makes the particle concentration become larger, resulting in a more significant turbulence

modulation. This unexpected result may be ascribed to the different interaction mechanisms between particles and turbulent coherent structure near the wall and in the logarithmic layer since the lift force is significant near the wall but negligible in the outer layer [see Fig. 3(b)]. The differences in turbulence modulations between inner and outer layers caused by the lift force will be further discussed in the next subsection.

D. Turbulent coherent structure

Figure 6 shows the conditionally averaged hairpin vortices in cases B and C. Linear stochastic estimation (LSE) is used to perform the conditional averaging [31,67]. We provide a brief description of LSE theory here. Given the target event $\mathbf{E}(\boldsymbol{x}^*)$ at location $\boldsymbol{x}^*$, the conditionally averaged velocity fluctuation $\boldsymbol{u}'$ at location $\boldsymbol{x}$ is expressed as $\langle \boldsymbol{u}' \mid \mathbf{E} \rangle$. LSE approximates the linearly estimated field $\widehat{u}(x)$ as $\hat{u}_i(\boldsymbol{x}) = L_{ij}(\boldsymbol{x}, \boldsymbol{x}^*)E_j(\boldsymbol{x}^*)$, where $L_{ij} = \langle E_j E_l \rangle^{-1} \langle u_i E_l \rangle$ represents, in a least-squares sense, the best linear approximation to the conditionally averaged $\langle \boldsymbol{u}' \mid \mathbf{E} \rangle$. In this paper, the target events are selected as the symmetric Q2 events ($u_1' < 0, u_2' > 0, u_3 \approx 0$) at $y^+ = 50$. In Fig. 6, the hairpin vortices are identified by the isosurface of 0.3 times the maximum λ_{ci} in the single-phase flow. Moreover, the contours show the conditionally averaged streamwise velocity fluctuation at $y^+ = 15$ [see Figs. 6(a), 6(c) and 6(e)] and particle distribution at $z^+ = 0$ [see Figs. 6(d) and 6(f)]. In Fig. 6(a), the low-speed streak is located between the counter-rotating legs of the Q2-based hairpin vortex, pulled away from the wall, redirected upwards and accompanied by the high-momentum fluid downstream of the vortex head, which corresponds to the ejection and sweep events respectively. With the addition of inertial particles, the shape of the conditional structures is relatively unchanged, though its extent is, on average, compressed due to the near-wall high particle concentration. The lowest height of the isosurface increases and the low-speed region is slightly extended [see Fig. 6(c)] as compared to the single-phase case. When the lift force acts on the particles, they are more evenly distributed in the entire domain. Figure 6(f) shows that particles are elevated upstream of the conditional eddy in the range $10 < y^+ < 100$. The local particle concentration between the hairpin legs and the vortex head is so high that the particle-vortex interaction destroys their connection. The two legs are separated for the chosen isosurface and the spacing between the legs becomes greater [see Fig. 6(e)].

Figure 7 presents the spanwise two-point correlations of the fluid streamwise velocity fluctuation $R_{u'u'}$ at $y^+ = 15$ and $y^+ = 52$ for cases B and C, as well as that for single-phase case. The spanwise separation at which the minimum of $R_{u'u'}$ occurs corresponds approximately to half the mean spacing of the streaks. The corresponding indicator lines (dashed line) of $R_{u'u'} = 0.2$ are also given in Fig. 7 to compare the spanwise scale of the streaks for different cases. For the inertial-particle case, the mean streak spacing is basically unchanged as compared with the single-phase case. It is about $\Delta z^+ = 120$ at $y^+ = 15$ and $\Delta z^+ = 200$ at $y^+ = 52$. However, these streaks become slightly wider in the spanwise direction, which is consistent with the results of Dritselis and Vlachos [30] and Picano *et al.* [68]. With the lift force, the particles significantly increase the mean width and spacing of the streaks both in the buffer layer and logarithmic layer due to the strong particle-fluid interaction. This result is consistent with Li *et al.* [32] who reported that the particles with $\mathrm{St}^+ = 9$ increase the spacing of the near-wall streaks, but inconsistent with their conclusion that the streak spacing is basically not affected by particles in the outer layer due to different conditions of upper boundary.

The above differences in particle distribution, turbulence statistics, and structure clearly demonstrate the influence of the lift force. To understand the underlying dynamics, we show the distributions of the particles around a coherent streamwise vortex, which rotates clockwise in the buffer layer, in the y^+-z^+ plane. The colored streamwise vorticity in all four diagrams is drawn as background, with a red bold arrow near the vortex core indicating its direction of rotation. The dot symbols indicate particle locations. The black arrows in Fig. 8(a) indicate the velocity vectors (u_{p2}^+, u_{p3}^+), while those in Fig. 8(c) indicate the force vectors (f_2^+, f_3^+) on the particles. It is seen that the turbulent coherent structures transport the particles from the outer layer to the wall

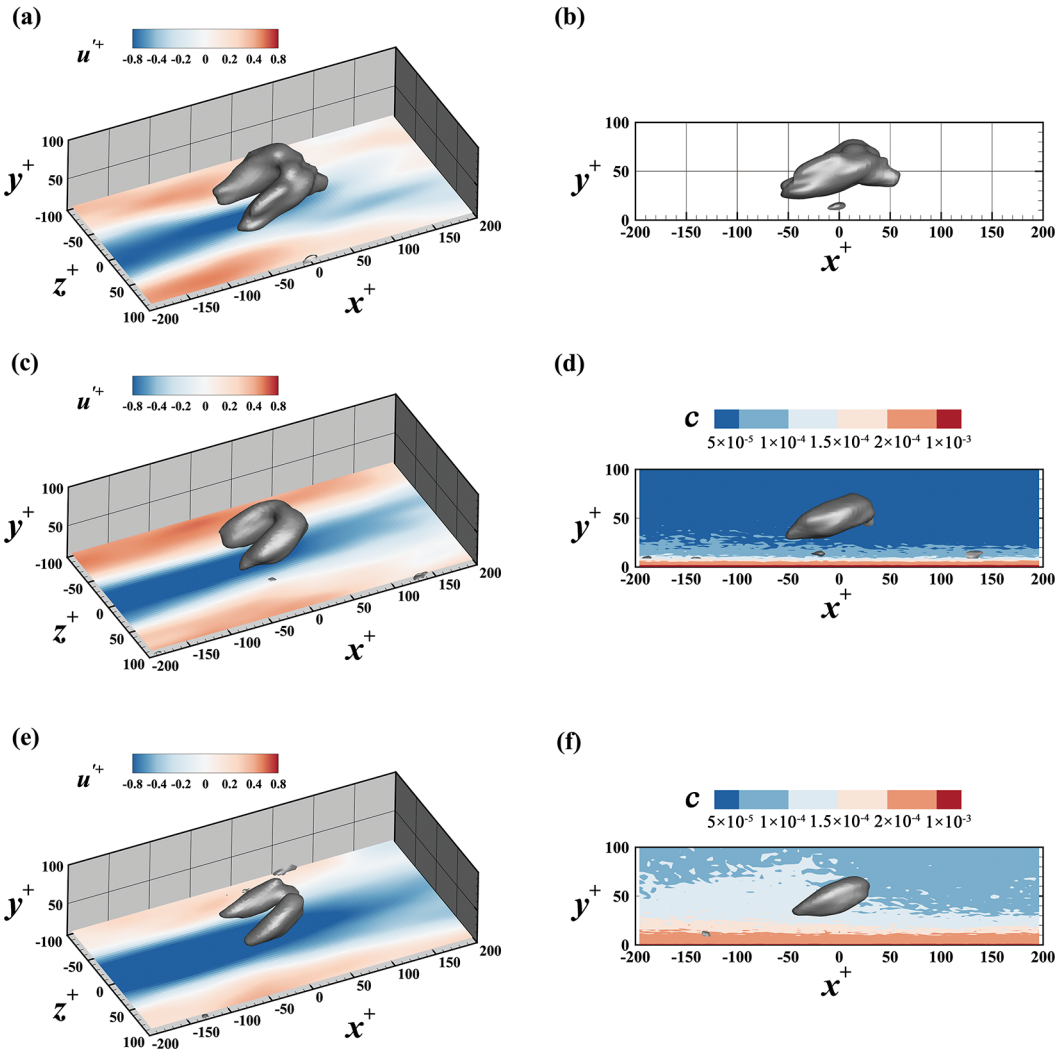

FIG. 6. Conditionally averaged hairpin vortex based on symmetric Q2 events ($u_1' < 0, u_2' > 0, u_3 \approx 0$) at $y^+ = 50$ for $\mathrm{Re}_\tau = 180$. The hairpin vortices are identified by the isosurface of 0.3 (0.31 in Zhou *et al.* [60] and 0.39 in Richter and Sullivan [31]) times the maximum λ_{ci} in the single-phase flow. Top row corresponds to single-phase flow, middle row corresponds to case C (without lift force), and bottom row corresponds to case B (with lift force). Horizontal slice in the left column is located at $y^+ = 15$ and the vertical slice in the right column is located at $z^+ = 0$. For the left column, the contours represent the conditionally averaged fluid streamwise velocity fluctuation. For the right column, the contours represent the conditionally averaged particle concentration.

by sweeping event and take them away from the wall by ejection. Many inertial particles remain trapped in the low-speed region, see the lower left corner of the two figures, leading to the high particle concentration in the viscous sublayer and lower part of the buffer layer [9]. Dritselis and Vlachos [30] also found that the particles ($\mathrm{St}^+ = 10$ and 25) efficiently follow the fluid motions and rotate around the vortices. Under the effect of the negative lift force near the wall, the particles impact the lower wall with higher wall-normal velocity and rebound to the buffer layer and above, see Figs. 8(b) and 8(d). In the viscous sublayer, the intensified crossing-trajectory effect due to

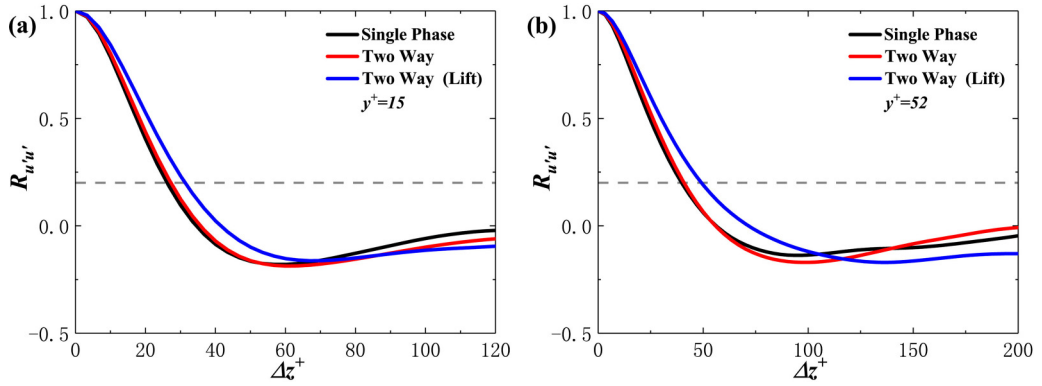

FIG. 7. Spanwise two-point correlations of the fluid streamwise velocity fluctuation at (a) $y^+ = 15$ and (b) $y^+ = 52$ for cases B and C. The dashed lines indicate $R_{u'u'} = 0.2$.

the more violent impact and rebound of particles near the wall makes the particle distribution more uniform (particles no longer apparently concentrate in the low-speed ejection events) and reduces the correlation between particle motion and the quasistreamwise vortex. The particles do not dominantly follow the fluid motions anymore. Instead, they may cross the vortex cores with a higher speed, and as a result, destroy the coherence of the vortex. The resultant of the lift and the drag force on a single particle in Fig. 8(d) usually deviates from its velocity vector. Therefore, the lift force further reduces the near-wall fluid velocity fluctuations compared to the case without

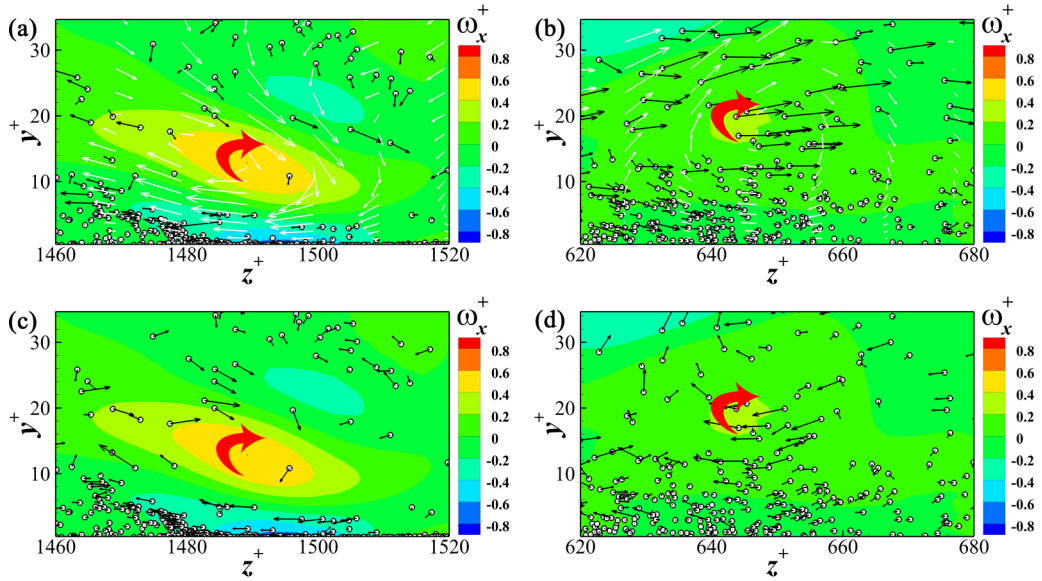

FIG. 8. Instantaneous flow field and particle distributions near a buffer-layer quasistreamwise vortex, which rotates clockwise, in the y^+-z^+ plane. The colored streamwise vorticity in all four diagrams are drawn as background, with a red bold arrow near the vortex core indicating its direction of rotation. Dot symbols indicate particle locations. The black arrows in panel (a) indicate the velocity vectors (u_{p2}^+, u_{p3}^+) for inertial particles in case C, while those in panel (c) indicate resultant force vectors (f_2^+, f_3^+) on them. The corresponding results for case B are shown in panels (b) and (d), respectively.

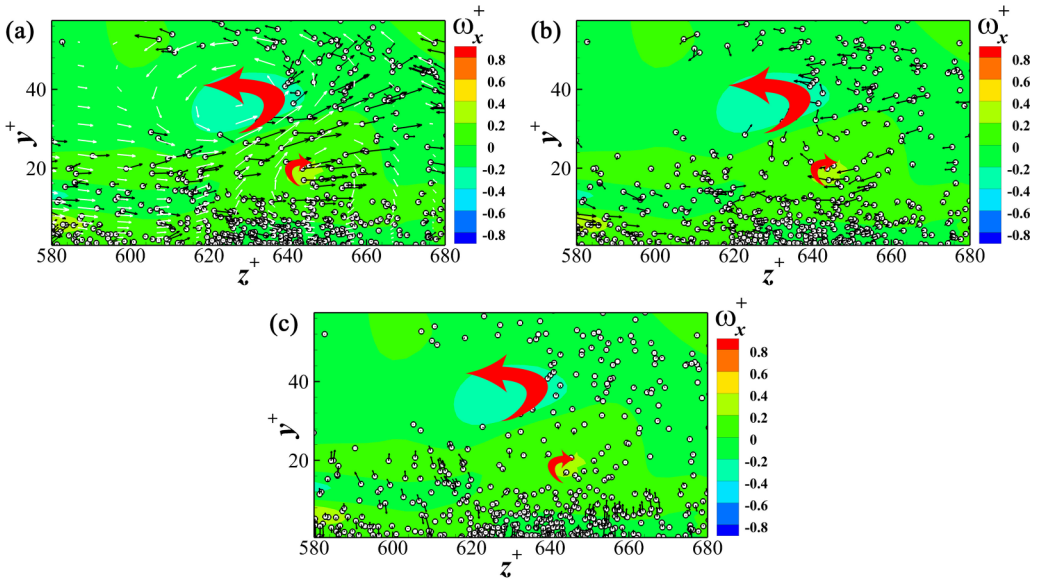

FIG. 9. The particle distribution (a), the drag force (b), and the lift force (c) at the same instant as Figs. 8(b) and 8(d), but within an enlarged field of vision. The black arrows in panel (a) indicate the vectors of (u_{p2}^+, u_{p3}^+). The same scale is used for the drag force and lift force vectors in panels (b) and (c).

the lift force [see Fig. 5(b)], though the particle concentration is lower [see Fig. 3(a)]. The above mechanisms can explain the reduction of the near-wall turbulent velocity fluctuation.

Finally, we further discuss the particle-turbulence interaction in the logarithmic layer for case B (two-way coupled simulation with the lift force). Figure 9 shows the instantaneous particle distribution, particle velocity and the force vectors at the same moment as Figs. 8(b) and 8(d), but within an enlarged field of vision. There is a counterclockwise rotating vortex in the upper left corner of the figure, which is paired with the buffer-layer clockwise rotating vortex. Figure 9(a) shows that the particles bouncing above the viscous sublayer can move upwards along the "channel" formed between the paired rotating vortices. In the logarithmic layer where the particles rarely experience the lift force due to the lower mean shear, they still gather around the counterclockwise vortex due to centrifugal force and move approximately tangentially along its rotation at this height. It is clear, by comparing Fig. 9(b) with Fig. 9(c), that the particle motion is dominated by the drag force. In any case, only under the action of the high shear lift force near the wall can more particles be transported into the logarithmic layer where they further enhance the streamwise turbulent fluctuation [see Fig. 5(b)].

E. Influence of Reynolds number

Since the Saffman force is proportional to the fluid shear, the importance of F_{Li} may increase with the increasing Reynolds number. Figure 10(a) shows the mean ratio of the lift force to the drag force acting on the particles in two-phase flow. The profiles of the ratio are similar at the two Reynolds numbers of $\mathrm{Re}_\tau = 180, 580$. The wall-normal lift force decreases with height in magnitude and dominates the other two components. As expected, the ratio of F_{L2}/F_{D2} increases with the increased turbulent Reynolds number in the viscous sublayer. However, the ratio of F_{Li}/F_{Di} shows less differences away from the wall at the two Reynolds numbers. Figure 10(b) shows the profiles of particle concentration for $\mathrm{Re}_\tau = 580$. As that in Fig. 3(a), particles are less accumulated near the wall when the Saffman force is involved. Note that the wall accumulation of inertial particles is already less apparent at high Reynolds number because the streamwise velocity

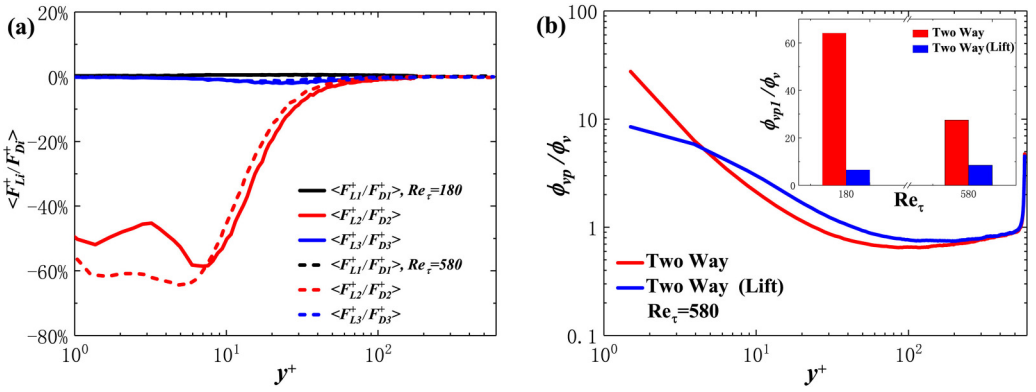

FIG. 10. (a) The mean ratio of the lift force to the drag force profiles with $St^+ = 31$ in the three directions for $Re_\tau = 180$ and 580. (b) The particle concentration profiles with $St^+ = 31$ for $Re_\tau = 580$ (inset represents the particle concentration ϕ_{vp1}/ϕ_v at the first statistical height).

fluctuation in the buffer layer increases with Re_τ [65,69], resulting in stronger low-speed streaks. Consequently, particles are easier to be entrained into the core region of turbulence by the ejection events. Figure 11 depicts the conditionally averaged hairpin vortex and particle concentration in its symmetric plane for cases at $Re_\tau = 580$. The Re_τ dependence of inertial particle distribution is clear by comparing Figs. 11(d) and 6(d). When the lift force is involved, the migration of particles to the central region of channel is more apparent [Fig. 11(f)] as compared to the low Reynolds number case [Fig. 6(f)]. It is also observed that the effect of particles on turbulent structures decrease with increasing Re_τ though the lift force plays similar role at the studied two Reynolds number. To quantify the effect of the lift force on the particle-turbulence interaction, we define a relative difference $D(Q) = D(Q)_L - D(Q)_{NL}$, where $D(Q)_L = (Q_L - Q_{SP})/Q_{SP} \times 100\%$ and $D(Q)_{NL} = (Q_{NL} - Q_{SP})/Q_{SP} \times 100\%$ represent the turbulence modulation in the cases with and without the lift force, respectively. Q are the particle and turbulence statistics and the subscripts "L," "NL," and "SP" represent the particle-laden cases with/without the lift force and single-phase flow, respectively. In particular, for the particle statistics, "SP" is replaced by "NL." We further show the relative differences for the streamwise component of particle and turbulent statistics at $Re_\tau = 180, 580$ in Figs. 12(a) and 12(b), respectively. Interestingly, the weaker influences of the Saffman force can be observed at higher Re_τ, which implies that the importance of the lift force to the particle motion and turbulence modulation is reduced at high Reynolds number. This is good news for future high-Re_τ investigations about the particle-fluid interaction, at least under the frame of two-way coupling and over a solid wall. However, the results also suggest that extra caution should be taken to quantitatively compare numerous previous studies at low Re_τ based on the various forces governing the particle motion. In addition, the influence of the lift force is more significant in the particle statistics as compared to turbulent statistics. From Figs. 10 and 12, we see a more-than-200% difference of the particle concentration and particle velocity fluctuation but just a less-than-10% difference of the fluid velocity fluctuation (partly because of the low ϕ_m) caused by the Saffman force.

Another interesting phenomenon is the Re_τ-dependence of particle accumulation concerning the coupling manner. In the one-way coupled PP-DNS of channel turbulence laden with inertial particles of similar Stokes number ($St^+ = 10$–100), Bernardini [23] found that the accumulation of inertial particles on the wall increases with Re_τ. As mentioned before, the inertial particles gradually accumulate near the wall due to turbophoresis [9,19,70]. Therefore, the mean turbophoretic velocity $\langle v_t^+ \rangle$ ($v_t^+ = -St^+ \partial \langle u_2'^{+2} \rangle / \partial y^+$, which is given by Caporaloni *et al.* [71]) in the region $y^+ < 15$ is calculated. For one-way coupled simulation, $\langle v_t^+ \rangle$ is -0.387 and -0.629 for $Re_\tau = 180$ and 580, respectively. This phenomenon can also explain the law found by Bernardini [23]. For two-way

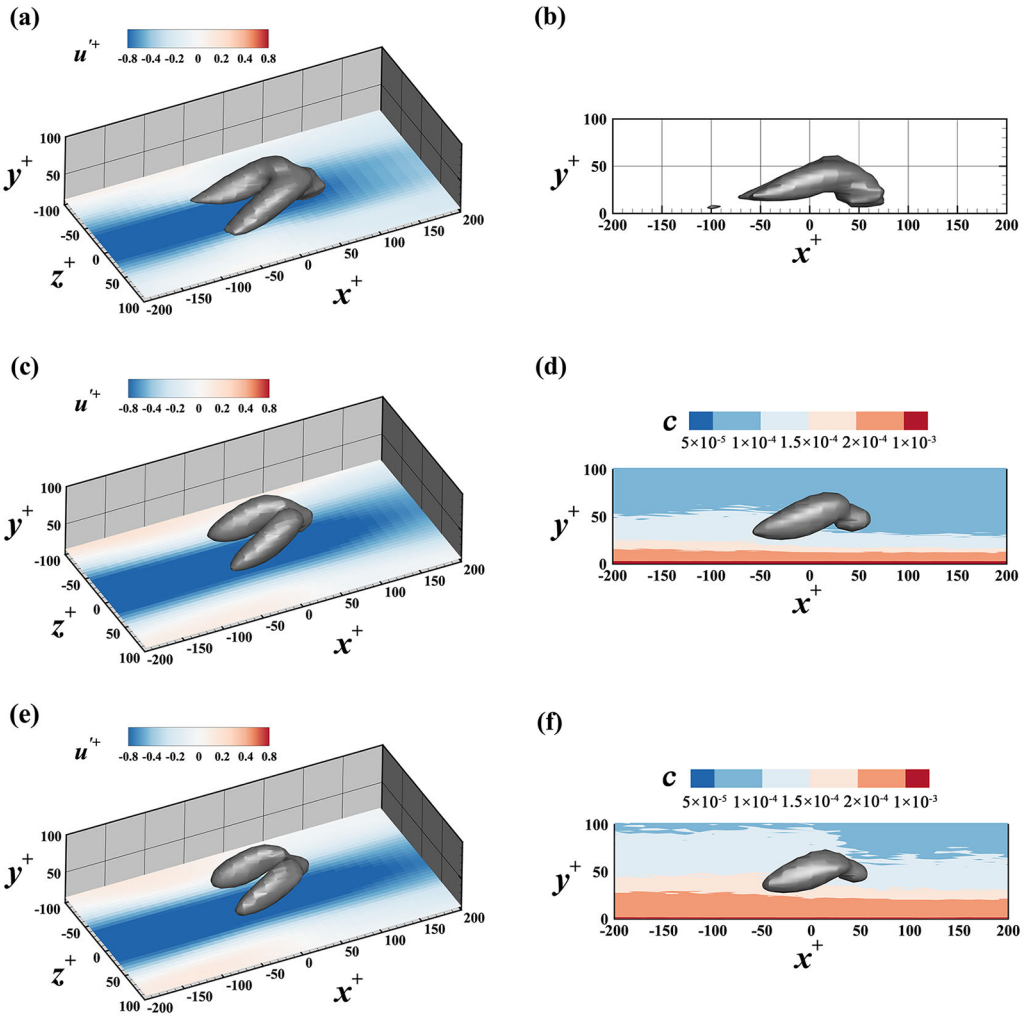

FIG. 11. Same as described in the caption of Fig. 6 but for $\mathrm{Re}_\tau = 580$.

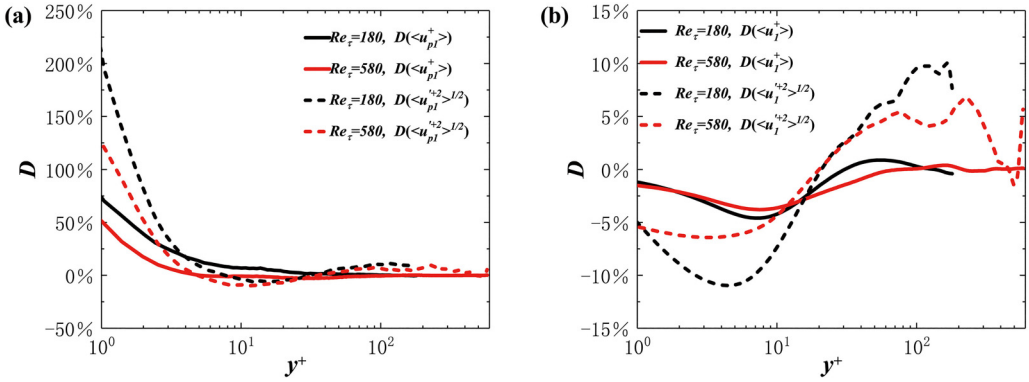

FIG. 12. The relative difference for the streamwise component of (a) particle statistics and (b) fluid statistics with $\mathrm{St}^+ = 31$ at $\mathrm{Re}_\tau = 180$ and 580.

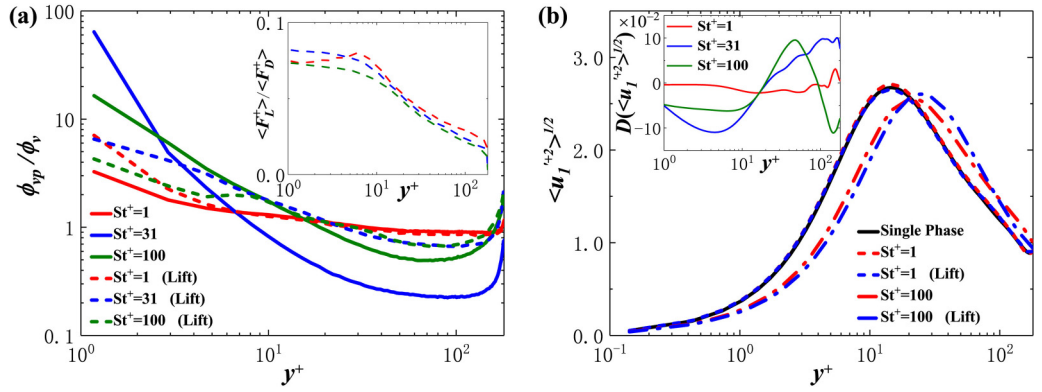

FIG. 13. (a) Particle concentration and (b) RMS streamwise fluid velocity fluctuation profiles with different inertial particle. The inset in panel (a) is the ratio profiles of the mean lift force to the mean drag force. The inset in panel (b) is the relative differences of RMS of streamwise fluid velocity fluctuation.

coupled cases, however, $\langle v_t^+ \rangle$ are -0.356 and -0.225 at the two Reynolds numbers, indicating that the turbophoresis in two-way coupled turbulence decreases with increasing Re_τ due to the interphase interaction. The inset in Fig. 10(b) shows the particle concentration ϕ_{vp1}/ϕ_v at the first statistical height in different cases. For $\mathrm{Re}_\tau = 180$, the near-wall concentration of inertial particle (case C) is up to 64.1. However, that of inertial particle (case I) is only 27.5 for $\mathrm{Re}_\tau = 580$, which is 57.1% smaller than case C. Further, involving the Saffman force in two-way coupled simulation of various Reynolds numbers results in the reduction of ϕ_{vp1}/ϕ_v itself, as shown in the inset of Fig. 10(b). ϕ_{vp1}/ϕ_v are 6.5 and 8.5 for $\mathrm{Re}_\tau = 180$ and 580, respectively, which is contrary to the law for inertial particles. Besides, the relative reduction of ϕ_{vp1}/ϕ_v is less pronounced at $\mathrm{Re}_\tau = 580$.

F. Influence of particle inertia

Previous studies based on just particle drag force have shown that particle inertia strongly affects the statistics of particles and turbulence [12,19,24,34,59]. Generally, the moderate-inertia particles have the maximum turbophoresis and accumulation. The present simulated results of the inertial particle in Fig. 13(a) suggest that the moderate-inertia particles with $\mathrm{St}^+ = 31$ accumulate the most near the wall as compared with low-inertia ($\mathrm{St}^+ = 1$) and high-inertia ($\mathrm{St}^+ = 100$) particles, which is the same as previous conclusions [24,59]. The low-inertia particles are most evenly distributed along the height. On the contrary, the near-wall concentration profile of the low-inertia particles with the Saffman force displays the fastest attenuation along height as compared with the other two cases, which agrees with Marchioli *et al.* [22]. This is because the low-inertia particles tend to follow the fluid [24]. Their slip velocity and lift force are not large enough to endow them with a sufficiently large rebound velocity after particle-wall collision. As a result, they will be trapped near the wall, just as their no-lift-force partners though the difference in near-wall concentration caused by the lift force is still visible. For moderate- and high-inertia particles, the effects of the lift force on the concentration profiles are similar. In addition, the inset of Fig. 13(a) shows that in the viscous sublayer, the ratio of the lift force to the drag force does not increase monotonically with increasing particle inertia. The moderate-inertia particles account for the largest lift force, which leads to the most significant change in the near-wall particle concentration.

Finally, Fig. 13(b) depicts the profiles of the RMS streamwise fluid velocity fluctuation for $\mathrm{St}^+ = 1$ and 100. The inset shows the relative differences with and without the lift force for three inertias [refer Fig. 5(b) for $\mathrm{St}^+ = 31$]. It is clear that the effect of the lift force on the streamwise fluid velocity fluctuation is very slight for the low inertial particles. However, for the moderate- and high-inertia particles, the lift force makes negative relative differences near the wall and positive

relative differences in the logarithmic layer as compared to the cases without lift force. Near the wall, the relationship between the influence of the lift force and particle inertia is nonmonotonic, moderate inertial particles are most affected by the lift force because of the largest ratio of the lift/drag force on particles.

IV. CONCLUSIONS

In this paper, the horizontal open-channel turbulences at friction Reynolds numbers of $\mathrm{Re}_\tau = 180, 580$ and laden with particles of various inertia ($\mathrm{St}^+ = 1, 31, 100$) are simulated. Besides the Stokes drag force, the Saffman force is included in the particle motion equation in several simulation cases. Therefore, the effects of the shear-induced lift force on particle distribution and turbulence modulation can be revealed by comparing against its no-lift-force partner. Meanwhile, we also discuss the influences of coupling manners and the significance of the shear-induced lift force for various particle inertias at various turbulent Reynolds numbers.

Since the particle-turbulence interaction is the most intense when particle response time is close to the certain characteristic timescale of turbulence, we first thoroughly analyze the simulated results for $\mathrm{Re}_\tau = 180$ and $\mathrm{St}^+ = 31$. In this case, under the effect of the negative lift force near the wall, particles impact the wall with higher wall-normal velocity and rebound faster to the buffer layer. They can further move upwards along the "channel" formed between the larger-scale paired rotating vortices in the logarithmic layer once escape the trapping effect of the wall. Therefore, the strong accumulation of the particles near the wall is suppressed by the lift force as compared to the case laden with inertial particles, resulting relatively uniform particle distribution in wall-normal direction. The resultants of the lift and the drag force on particles usually deviate from their velocity vector, preventing them from following the fluid motions. On the contrary, particles are easy to cross the vortex core. Consequently, the preferential concentration in the low-speed streaks near the wall is suppressed. In the outer layer, particles with lift force also tend to distribute in the high-speed regions due to the centrifugal effect and relatively small lift force.

By the same token, the near-wall turbulent velocity fluctuations are further suppressed in spite of the lower concentration there as compared to case laden with inertial particles. In the outer layer, the modulation of turbulent intensities when considering the lift force is enhanced because of the higher particle concentration. Through comparing the conditionally averaged hairpin vortex and spanwise two-point correlations of the fluid streamwise velocity fluctuation, we conclude that inertial particles reduce the scale of the hairpin vortex and increase the spacing of turbulent streaks. This phenomenon is more pronounced when the lift force is involved due to the intensified crossing-trajectory effect, which in turn explains the near-wall changes in turbulent intensities.

In addition, we also find that the effects of the lift force on particle statistics are more pronounced in one-way coupling simulation, the lift force is less significant at high Reynolds number in the context of turbulent modulation and even with the shear-induced lift force, the particle-turbulence interaction is still the strongest for the moderate-inertia particle.

It should be pointed out that we overlooked the gravity and interparticle collisions because the simulations are limited in high Fr_p and low ϕ_v. Our future work will further focus on the effects of the gravity and interparticle collisions on the particle-turbulence interaction, in addition to the dependence on Stokes number and Reynolds number.

ACKNOWLEDGMENTS

The authors acknowledge the National Natural Science Foundation of China (No. 12388101, No. 92052202, and No. 12072138), the National Key Scientific and Technological Infrastructure project "Earth System Numerical Simulation Facility" (EarthLab), and Natural Science Foundation of Gansu Province (No. 23JRRA1035).

APPENDIX A: INTRODUCTION AND COMPARISON OF SAFFMAN LIFT FORCE MODELS

The Saffman lift force was first obtained in a uniform simple shear flow laden with a moving sphere at low Reynolds numbers Re_p and Re_ω ($= d_p^2|\omega|/v$) and high ε ($= \mathrm{Re}_\omega^{0.5}/\mathrm{Re}_p$) in 1960s [1,2]. In the next few decades, many correction expressions have been put forward on the basis of Saffaman model (see Table II). Mclaughlin [72] extended Saffman's analysis to other asymptotic cases in which ε could reach ~20. Mei [73] proposed a modified form of Saffaman lift force for relatively high Re_p (~100). Kurose and Komori [78] even extended Re_p to 500. McLaughlin [75] and Cherukat and Mclaughlin [77] considered the effect of wall in wall-bounded linear shear flows. In their expressions, the distance between the particles and the wall is one of the key parameters. Besides, Giusti *et al.* [79] proposed a combination of Mclaughlin91 and KK model based on different Re_p.

Despite the variety of Saffman lift force models mentioned above, it is unclear which is the best choice. Costa *et al.* [36,37] tested two widely used shear-induced lift force models, Saffman model [1,2] and McLaughlin91 model [72]. They found that the PP-DNSs using both Saffman model or McLaughlin91 model are closer to PR-DNSthan those without shear lift force. The former lift force model predicts the vertical fluctuation and Reynolds stress of particles better (except for the height especially close to the wall) and the latter predicts other statistics better. Rousta *et al.* [39] compared the results of PP-DNS with the experimental observations in the vertical channel and also found the same effect of Saffman model and McLaughlin91 model as Costa *et al.* [36,37]. Accordingly, the differences between the simulations using Saffman model and the McLaughlin91 model ($\mathrm{Re}_\tau = 180$, $\mathrm{St}^+ = 31$, $d_p = 0.47\eta$, $\rho_p/\rho_f = 1550$) are briefly compared. Note that $\widetilde{\boldsymbol{\omega}}$ is obtained by the trilinear interpolation. Figure 14 shows the profiles of particle and fluid statistics. The influence trend using the two different models is qualitatively consistent. The two models both reduce the particle aggregation, increase the mean velocity and streamwise fluctuation of particle, and suppress the streamwise fluctuation of fluid as compared with inertial particle. That is why we just deploy Saffman model in the simulation. However, it should be noted that the conclusions about model comparison in this paper only apply to the particles with high density ratio. For very light particles (e.g., microbubbles with density ratio much less than 1), the impact of the lift models might be different, especially in the high shear region [80].

APPENDIX B: MODEL EVALUATIONS

The numerical results are compared with previous studies to evaluate the code. Since the numerical results with $\mathrm{Re}_\tau = 580$ have already been verified in Wang *et al.* [29], only those with $\mathrm{Re}_\tau = 180$ are discussed here. Figure 15(a) shows the root-mean-square (RMS) of fluid velocity fluctuations $\langle u_i'^+ u_i'^+ \rangle^{1/2}$ and the Reynolds stress $\langle u_1'^+ u_2'^+ \rangle$ for the single-phase case at $\mathrm{Re}_\tau = 180$. The simulated results are in full agreement with the DNS statistics of Lee and Moser [65]. The particle velocity fluctuations from an additional simulation of particle-laden flow one-way coupled with 500 000 particles of $\mathrm{St}^+ = 50$ is compared with Costa *et al.* [37] in Fig. 15(b). With the same parameters, our results agree well with those of Costa *et al.* [37]. Finally, Fig. 15(c) shows the RMS of the streamwise fluid velocity fluctuation for case C (two-way coupled simulation of turbulence laden with inertial particles). The results of Lee and Lee [27] ($\mathrm{St}^+ = 21.2$, $\rho_p/\rho_f = 833$, $\phi_v = 2.4\times10^{-4}$) and Zhao *et al.* [26] ($\mathrm{St}^+ = 30$, $\rho_p/\rho_f = 1041$, $\phi_v = 2.9\times10^{-4}$) with similar particle parameters are presented. All three curves are in general agreement, proving the reliability of the code and models.

APPENDIX C: DIFFERENT TWO-WAY COUPLING METHODS

The method for two-way coupling is pivotal in simulating of two-phase flow. There are several methods available, such as PSI-CELL, Gaussian kernel, ERPP, etc.

In the PSI-CELL method [57], the interphase momentum transfer term is calculated as the summation of feedback forces exerted on the fluid by each particle in the control volume surrounding a grid node. Although the feedback force exhibits grid dependency when the number of particles

TABLE II. Shear lift models and their restrictive parameters. $\boldsymbol{U}_s = \tilde{\boldsymbol{U}} - \boldsymbol{U}_p$ represents the slip velocity between local fluid and particle. $\tilde{\boldsymbol{\omega}}$ represents the local fluid vorticity at the particle position. The shear Reynolds number is defined as $\mathrm{Re}_\omega = d_p^2|\omega|/v$. The parameter ε is defined as $\varepsilon = \mathrm{Re}_\omega^{0.5}/\mathrm{Re}_p$. $\beta = \mathrm{Re}_\omega/2\mathrm{Re}_p$, $\Lambda = d_p du_1/2dy|\boldsymbol{U}_s|$, $\alpha = \partial\langle|\boldsymbol{U}_s|\rangle/\partial y$ and $\kappa = d_p/2y_p$.

Reference	Method	Experssion	Restrictive parameter	Abbreviation	Application	Focus
Saffman [1,2]	theory	$\boldsymbol{F}_L = 1.615J\mu d_p\lvert\boldsymbol{U}_s\rvert\sqrt{\frac{d_p^2\lvert\tilde{\boldsymbol{\omega}}\rvert}{v}}\frac{\boldsymbol{U}_s\times\tilde{\boldsymbol{\omega}}}{\lvert\tilde{\boldsymbol{\omega}}\rvert\lvert\boldsymbol{U}_s\rvert}$ $J = 1.0$	$\mathrm{Re}_p \ll 1$ $\mathrm{Re}_\omega \ll 1$ $\varepsilon \gg 1$	Saffman model	McLaughlin [3] Zhang and Ahmadi [4] Costa *et al.* [37]	particle deposition particle deposition particle deposition[a]
Mclaughlin [72]	theory	$J_{Mc} = 0.3\left(1+\tanh\left[\frac{5}{2}(\log_{10}\varepsilon + 0.191)\right]\right)\left(\frac{2}{3}+\tanh(6\varepsilon - 1.92)\right)$	$\mathrm{Re}_p \ll 1$ $\mathrm{Re}_\omega \ll 1$	Mclaughlin91 model	Marchioli and Soldati [9] Costa *et al.* [37] Rousta *et al.* [39]	particle deposition[a] particle deposition[a] particle deposition[a]
Mei [73]	simulation	$J = \begin{cases}(1-0.3314\beta^{\frac{1}{2}})\exp(-\frac{\mathrm{Re}_p}{10}) \\ +0.3314\beta^{1/2} \\ 0.0524(\beta\mathrm{Re}_p)^{1/2}\end{cases}$	$0 \leqslant \alpha \leqslant 0.4$ $\mathrm{Re}_p \leqslant 40$ $40 < \mathrm{Re}_p \leqslant 100$	Mei model	Li *et al.* [32] Li *et al.* [5] Mortimer *et al.* [6] Mortimer and Fairweather [41] Chen *et al.* [74]	turbulence modulation turbulence modulation particle deposition turbulence modulation turbulence modulation
McLaughlin [75]	theory	$J = \begin{cases}\frac{\pi^2}{16}(\frac{1}{\varepsilon}+\frac{11}{6}y_p^+) \\ J_{Mc} - \frac{1.879}{(y_p^+)^{5/3}}\end{cases}$	$y_p^+ \leqslant 5$ $y_p^+ > 5$	Mclaughlin93 model	Chen and Mclaughlin [76] Nasr *et al.* [40]	particle deposition turbulence modulation
Cherukat and Mclaughlin [77]	theory	$F_L = 0.25\rho_f d_p^2 U_s^2 I$ $I = 1.7716 + 0.2160\kappa - 0.7292\kappa^2 + 0.4854\kappa^3 - (3.2397\kappa^{-1} + 1.1450 + 2.0840\kappa - 0.9059\kappa^2)\Lambda + (2.0069 + 1.0575\kappa - 2.4007\kappa^2 + 1.3174\kappa^3)\Lambda^2$	$\kappa \approx 1$	CM model	Wang *et al.* [62] Arcen, Tanière, and Oesterlé [7]	particle deposition[a] particle deposition[a]
Kurose and Komori [78]	simulation	$F_L = \frac{1}{8}C_L\rho_f U_s^2 \pi d_p^2$ $C_L = K_0\alpha^{0.9} + K_1\alpha^{1.1}$	$0 \leqslant \alpha \leqslant 0.4$ $1 < \mathrm{Re}_p \leqslant 500$	KK model	Marchioli *et al.* [22]	particle deposition[a]
Giusti *et al.* [79]	interpolation	$J = \begin{cases}J_{Mc} \\ J_{Mc}\frac{5-\mathrm{Re}_p}{4} + J_{KK}\frac{\mathrm{Re}_p-1}{4} \\ J_{KK}\end{cases}$	$\mathrm{Re}_p < 1$ $1 < \mathrm{Re}_p < 5$ $\mathrm{Re}_p > 5$	GLS model	Marchioli *et al.* [22]	particle deposition[a]

[a]indicates that the comparison of cases with and without lift force is considered in the studies.

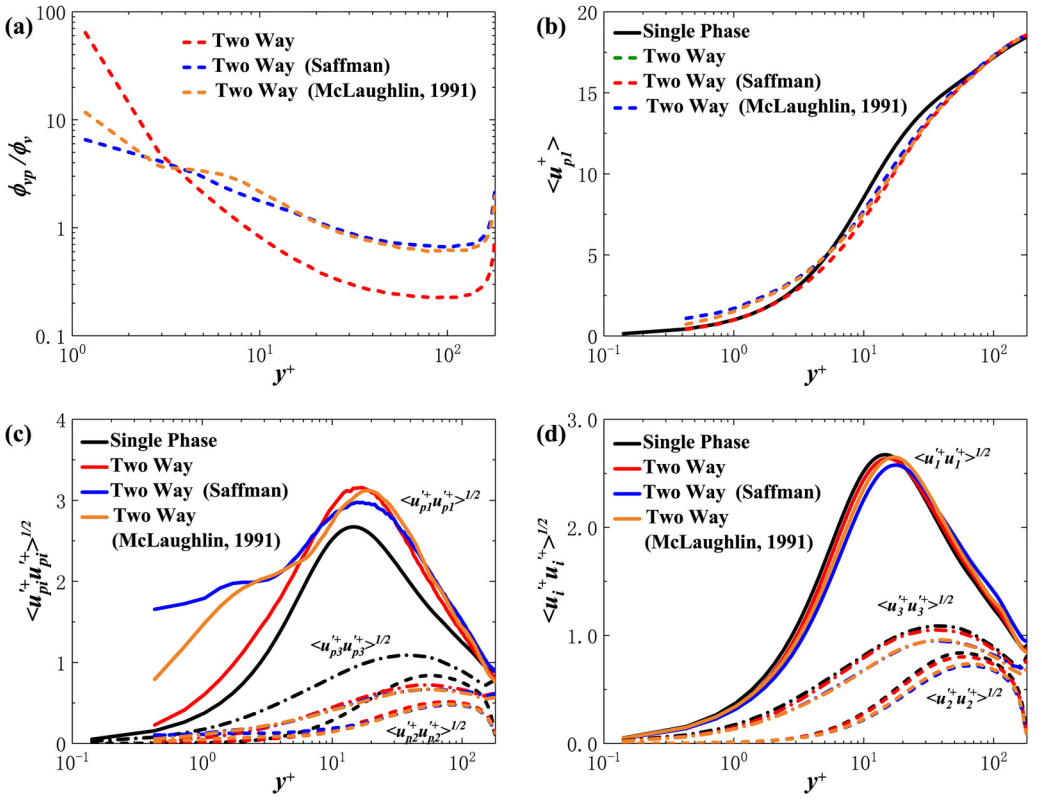

FIG. 14. The profiles of particle and fluid statistics of (a) particle concentration, (b) mean particle velocity, (c) particle velocity fluctuations, and (d) fluid velocity fluctuations.

per cell is insufficient [27,81,82], the method is relatively easy to perform. In addition, the method has been applied to many previous studies of two-phase channel turbulence [26,28,41,83,84], which facilitates comparison of different simulation results with similar parameters.

In the ERPP method [51], a regularization procedure with a temporal cutoff ϵ_R (the regularization diffusion timescale) is added to the Gaussian kernel method ($\mathrm{g}(\boldsymbol{x}-\boldsymbol{x}_p(t)) = \exp(-|\boldsymbol{x}-\boldsymbol{x}_p(t)|^2/2\sigma_R)/(\sigma_R\sqrt{2\pi})$, where σ_R is the bandwidth of the Gaussian kernel which indicates the size of the region influenced by a particle). The hydrodynamic force on the regularized solution at time t is the one experienced by the particle at a previous time $t-\epsilon_R$ when its position was $\boldsymbol{x}_p(t-\epsilon_R)$. The two-way force can be expressed as

$$\boldsymbol{f} = \sum_{p}^{n_p} \boldsymbol{F}(t-\epsilon_R) g[\boldsymbol{x}-\boldsymbol{x}_p(t-\epsilon_R), \epsilon_R]. \tag{C1}$$

There are two key parameters in the REPP method, namely, the bandwidth of the Gaussian kernel σ_R and the regularization diffusion timescale ϵ_R. For the parameters used in our simulations, $\sigma_R^+ = \Delta x^+ = 4.42(14.2)$, $\epsilon_R^+ = \sigma_R^{+2}/2 = 9.76(100.82)$ and hence 121 and 2520 instantaneous feedback force fields should be stored for simulation cases at Reynolds numbers 180 and 580. It is a very big challenge.

To implement the ERPP method, we artificially reduced the regularization diffusion timescale to 10 instantaneous feedback force fields and compared the effects of PSI-CELL and REPP methods based on turbulent statistics for case C ($\mathrm{Re}_\tau = 180$ and $\mathrm{St}^+ = 31$). The profiles of mean fluid

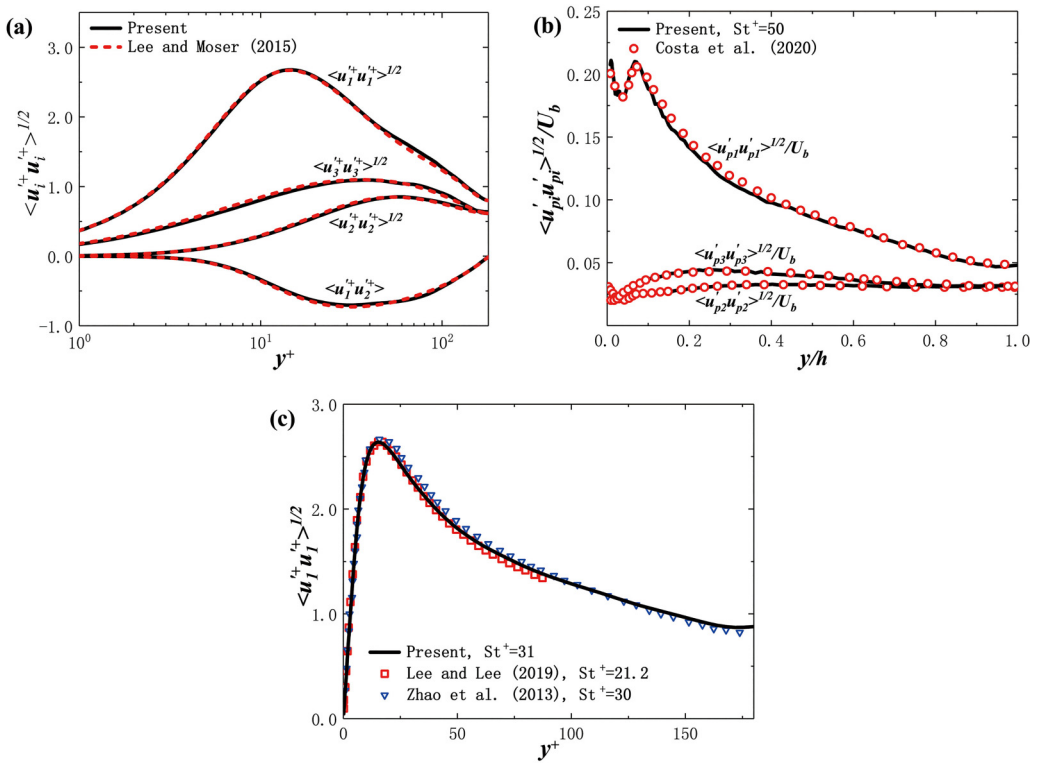

FIG. 15. (a) The root-mean-square (RMS) of fluid velocity fluctuations and Reynolds shear stress for the single-phase flow, (b) the RMS of particle velocity fluctuations for additional one-way coupled simulation, and (c) the RMS of streamwise fluid velocity fluctuation for case C ($\mathrm{Re}_\tau = 180$), compared with two previous simulations under similar parameter conditions.

velocity and RMS of fluid velocity fluctuations are shown in Fig. 16. It is seen that the results by the REPP method with reduced regularization diffusion time show a slight decrease of the streamwise turbulence intensity as compared to those by the PSI-CELL method. However, the two results are qualitatively consistent. For $\langle u_1'^+ \rangle$, $\langle u_2'^+ u_2'^+ \rangle$ and $\langle u_3'^+ u_3'^+ \rangle$, these two methods report slightly imperceptible differences.

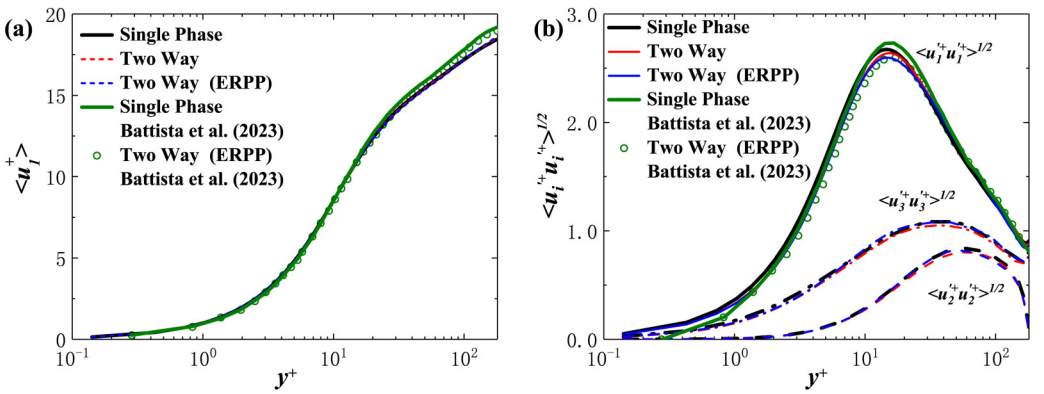

FIG. 16. The profiles of (a) mean fluid velocity and (b) RMS of fluid velocity fluctuations ($\mathrm{Re}_\tau = 180$, $\mathrm{St}^+ = 31$).

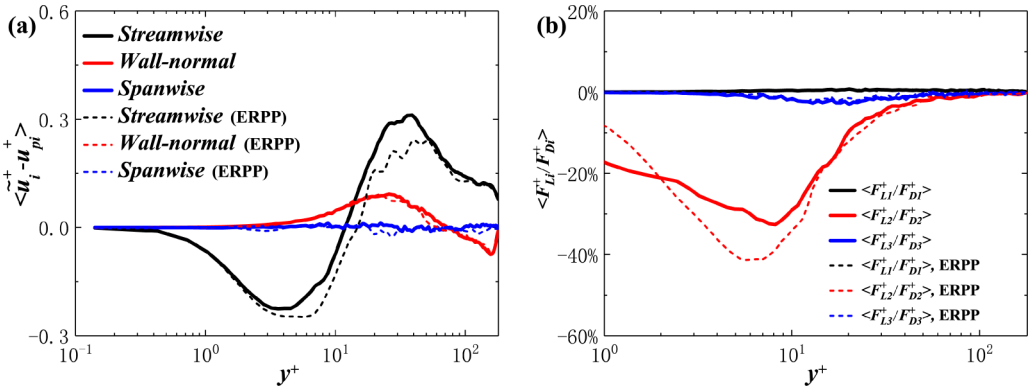

FIG. 17. The profiles of (a) mean slip velocity and (b) ratio of the virtual lift force to the drag force ($\mathrm{Re}_\tau = 180$, $\mathrm{St}^+ = 31$).

Battista *et al.* [56] simulated the two-way coupled turbulent pipe flows ($\mathrm{Re}_\tau = 180$) with different particle Stokes numbers ($\mathrm{St}^+ = 10 \sim 80$), mass loading ($\phi_m = 0 \sim 0.6$) and particle-to-fluid density ratio ($\rho_p/\rho_f = 90 \sim 560$) by using the ERPP method. They studied the effects of particles on the mean and fluctuating velocities of turbulence. The particle parameters of case C ($\mathrm{Re}_\tau = 180$, $\mathrm{St}^+ = 31$, $\phi_m = 0.18$, without lift force) in our manuscript are close to their low inertial and low mass-loading case ($\mathrm{St}^+ = 10$, $\phi_m = 0.2$). The results of Battista *et al.* [56] are also shown in the Fig. 16. It can be seen that our results by ERPP (with reduced diffusion timescale) exhibit similar modulation behaviors to that of Battista *et al.* [56].

Furthermore, we calculate the mean slip velocity and ratio of the virtual lift force (it is only calculated by the slip velocity and fluid vorticity at the particles but doesn't act on the particles) to the drag force based on the same cases shown in Fig. 16. As shown in Fig. 17, the ERPP method does influence the mean slip velocity (especially in streamwise direction) and the lift-to-drag force ratio in the near-wall region, but no qualitative difference can be observed. Therefore, we believe that the drawbacks of PSI-CELL method have no significant effect on the relative importance of lift force in our simulations. Whatever, the ERPP method, when solving the memory requirements at high Reynolds numbers, is a very promising method.

[1] P. G. Saffman, The lift on a small sphere in a slow shear flow, J. Fluid Mech. **22**, 385 (1965).
[2] P. G. Saffman, The lift on a small sphere in a slow shear flow—Corrigendum, J. Fluid Mech. **31**, 624 (1968).
[3] J. B. McLaughlin, Aerosol particle deposition in numerically simulated channel flow, Phys. Fluids **1**, 1211 (1989).
[4] H. Zhang and G. Ahmadi, Aerosol particle transport and deposition in vertical and horizontal turbulent duct flows, J. Fluid Mech. **406**, 55 (2000).
[5] D. Li, A. Wei, K. Luo, and J. Fan, Direct numerical simulation of a particle-laden flow in a flat plate boundary layer, Int. J. Multiphase Flow **79**, 124 (2016).
[6] L. F. Mortimer, D. O. Njobuenwu, and M. Fairweather, Near-wall dynamics of inertial particles in dilute turbulent channel flows, Phys. Fluids **31**, 063302 (2019).
[7] B. Arcen, A. Tanière, and B. Oesterlé, On the influence of near-wall forces in particle-laden channel flows, Int. J. Multiphase Flow **32**, 1326 (2006).
[8] J. Young and A. Leeming, A theory of particle deposition in turbulent pipe flow, J. Fluid Mech. **340**, 129 (1997).

[9] C. Marchioli and A. Soldati, Mechanisms for particle transfer and segregation in a turbulent boundary layer, J. Fluid Mech. **468**, 283 (2002).
[10] T. Zahtila, L. Chan, A. Ooi, and J. Philip, Particle transport in a turbulent pipe flow: Direct numerical simulations, phenomenological modelling, and physical mechanisms, J. Fluid Mech. **957**, A1 (2023).
[11] S. Balachandar and J. K. Eaton, Turbulent dispersed multiphase flow, Annu. Rev. Fluid Mech. **42**, 111 (2010).
[12] F. Battista, J. P. Mollicone, P. Gualtieri, R. Messina, and C. M. Casciola, Exact regularised point particle (ERPP) method for particle-laden wall-bounded flows in the two-way coupling regime, J. Fluid Mech. **878**, 420 (2019).
[13] Z. Zhu, R. Hu, Y. Lei, L. Shen, and X. Zheng, Particle resolved simulation of sediment transport by a hybrid parallel approach, Int. J. Multiphase Flow **152**, 104072 (2022).
[14] V. Armenio and V. Fiorotto, The importance of the forces acting on particles in turbulent flows, Phys. Fluids **13**, 2437 (2001).
[15] Y. Ling, M. Parmar, and S. Balachandar, A scaling analysis of added-mass and history forces and their coupling in dispersed multiphase flows, Int. J. Multiphase Flow **57**, 102 (2013).
[16] S. Pedinotti and G. Mariotti, Direct numerical simulation of particle behaviour in the wall region of turbulent flows in horizontal channels, Int. J. Multiphase Flow **18**, 927 (1992).
[17] M. Picciotto, C. Marchioli, and A. Soldati, Characterization of near-wall accumulation regions for inertial particles in turbulent boundary layers, Phys. Fluids **17**, 098101 (2005).
[18] A. Soldati and C. Marchioli, Physics and modelling of turbulent particle deposition and entrainment: Review of a systematic study, Int. J. Multiphase Flow **35**, 827 (2009).
[19] G. Sardina, P. Schlatter, L. Brandt, F. Picano, and C. M. Casciola, Wall accumulation and spatial localization in particle-laden wall flows, J. Fluid Mech. **699**, 50 (2012).
[20] Y. Jie, Z. Cui, C. Xu, and L. Zhao, On the existence and formation of multi-scale particle streaks in turbulent channel flows, J. Fluid Mech. **935**, A18 (2022).
[21] M. W. Reeks, The transport of discrete particles in inhomogeneous turbulence, J. Aerosol Sci. **14**, 729 (1983).
[22] C. Marchioli, M. Picciotto, and A. Soldati, Influence of gravity and lift on particle velocity statistics and transfer rates in turbulent vertical channel flow, Int. J. Multiphase Flow **33**, 227 (2007).
[23] M. Bernardini, Reynolds number scaling of inertial particle statistics in turbulent channel flows, J. Fluid Mech. **758**, R1 (2014).
[24] J. Lee and C. Lee, Modification of particle-laden near-wall turbulence: Effect of Stokes number, Phys. Fluids **27**, 023303 (2015).
[25] L. Zhao and H. I. Andersson, On particle spin in two-way coupled turbulent channel flow simulations, Phys. Fluids **23**, 093302 (2011).
[26] L. Zhao, H. I. Andersson, and J. J. Gillissen, Interphasial energy transfer and particle dissipation in particle-laden wall turbulence, J. Fluid Mech. **715**, 32 (2013).
[27] J. Lee and C. Lee, The effect of wall-normal gravity on particle-laden near-wall turbulence, J. Fluid Mech. **873**, 475 (2019).
[28] T. Zhou, L. Zhao, W. Huang, and C. Xu, Non-monotonic effect of mass loading on turbulence modulations in particle-laden channel flow, Phys. Fluids **32**, 043304 (2020).
[29] P. Wang, J. Li, and X. Zheng, The effect of gravity on turbulence modulation in particle-laden horizontal open channel flow, Phys. Fluids **33**, 083315 (2021).
[30] C. D. Dritselis and N. S. Vlachos, Numerical investigation of momentum exchange between particles and coherent structures in low Re turbulent channel flow, Phys. Fluids **23**, 025103 (2011).
[31] D. H. Richter and P. P. Sullivan, Modification of near-wall coherent structures by inertial particles, Phys. Fluids **26**, 103304 (2014).
[32] D. Li, K. Luo, and J. Fan, Modulation of turbulence by dispersed solid particles in a spatially developing flat-plate boundary layer, J. Fluid Mech. **802**, 359 (2016).
[33] G. Wang and D. H. Richter, Modulation of the turbulence regeneration cycle by inertial particles in planar Couette flow, J. Fluid Mech. **861**, 901 (2019).

[34] G. Wang and D. H. Richter, Two mechanisms of modulation of very-large-scale motions by inertial particles in open channel flow, J. Fluid Mech. **868**, 538 (2019).
[35] W. Gao, R. Samtaney, and D. H. Richter, Direct numerical simulation of particle-laden flow in an open channel at $\mathrm{Re}_\tau = 5186$, J. Fluid Mech. **957**, A3 (2023).
[36] P. Costa, L. Brandt, and F. Picano, Interface-resolved simulations of small inertial particles in turbulent channel flow, J. Fluid Mech. **883**, A54 (2020).
[37] P. Costa, L. Brandt, and F. Picano, Interface-resolved simulations of small inertial particles in turbulent channel flow, J. Fluid Mech. **891**, E2 (2020).
[38] R. Barati, S. A. A. S. Neyshabouri, and G. Ahmadi, Issues in Eulerian–Lagrangian modeling of sediment transport under saltation regime, Int. J. Sediment Res. **33**, 441 (2018).
[39] F. Rousta, B. Lessani, and G. Ahmadi, Particle dispersion and deposition in wall-bounded turbulent flow, Int. J. Multiphase Flow **158**, 104307 (2023).
[40] H. Nasr, G. Ahmadi, and J. B. McLaughlin, A DNS study of effects of particle-particle collisions and two-way coupling on particle deposition and phasic fluctuations, J. Fluid Mech. **640**, 507 (2009).
[41] L. F. Mortimer and M. Fairweather, Density ratio effects on the topology of coherent turbulent structures in two-way coupled particle-laden channel flows, Phys. Fluids **32**, 103302 (2020).
[42] K. Kim, S. J. Baek, and H. J. Sung, An implicit velocity decoupling procedure for the incompressible Navier-Stokes equations, Int. J. Numer. Meth. Fluids **38**, 125 (2002).
[43] T. S. Park and H. J. Sung, A nonlinear low-Reynolds-number κ-ϵ model for turbulent separated and reattaching flows—I. Flow field computations, Int. J. Heat Mass Transfer **38**, 2657 (1995).
[44] T. S. Park and H. J. Sung, Development of a near-wall turbulence model and application to jet impingement heat transfer, Int. J. Heat Mass Transfer **22**, 10 (2001).
[45] R. D. Moser, J. Kim, and N. N. Mansour, Direct numerical simulation of turbulent channel flow up to $\mathrm{Re}_\tau = 590$, Phys. Fluids **11**, 943 (1999).
[46] X. Zheng, S. Feng, and P. Wang, Modulation of turbulence by saltating particles on erodible bed surface, J. Fluid Mech. **918**, A16 (2021).
[47] Y. Li, J. B. McLaughlin, K. Kontomaris, and L. Portela, Numerical simulation of particle-laden turbulent channel flow, Phys. Fluids **13**, 2957 (2001).
[48] C. D. Dritselis and N. S. Vlachos, Numerical study of educed coherent structures in the near-wall region of a particle-laden channel flow, Phys. Fluids **20**, 055103 (2008).
[49] M. R. Maxey and J. J. Riley, Equation of motion for a small rigid sphere in a nonuniform flow, Phys. Fluids **26**, 883 (1983).
[50] L. Zhao, C. Reddy, H. I. Andersson, and E. A. Variano, Mapping spheroid rotation modes in turbulent channel flow: Effects of shear, turbulence and particle inertia, J. Fluid Mech. **876**, 19 (2019).
[51] P. Gualtieri, F. Picano, G. Sardina, and C. M. Casciola, Exact regularized point particle method for multiphase flows in the two-way coupling regime, J. Fluid Mech. **773**, 520 (2015).
[52] J. Horwitz and A. Mani, Accurate calculation of stokes drag for point-particle tracking in two-way coupled flows, J. Comput. Phys. **318**, 85 (2016).
[53] S. Balachandar, K. Liu, and M. Lakhote, Self-induced velocity correction for improved drag estimation in Euler-Lagrange point-particle simulations, J. Comput. Phys. **376**, 160 (2019).
[54] J. Horwitz and A. Mani, Correction scheme for point-particle models applied to a nonlinear drag law in simulations of particle-fluid interaction, Int. J. Multiphase Flow **101**, 74 (2018).
[55] M. Mehrabadi, J. Horwitz, S. Subramaniam, and A. Mani, A direct comparison of particle-resolved and point-particle methods in decaying turbulence, J. Fluid Mech. **850**, 336 (2018).
[56] F. Battista, P. Gualtieri, J.-P. Mollicone, F. Salvadore, and C. M. Casciola, Drag increase and turbulence augmentation in two-way coupled particle-laden wall-bounded flows, Phys. Fluids **35**, 045133 (2023).
[57] C. T. Crowe, M. P. Sharma, and D. E. Stock, The particle-source-in cell (PSI-CELL) model for gas-droplet flows, J. Fluids Engng **99**, 325 (1977).
[58] Q. Pan, H. Xiang, Z. Wang, H. I. Andersson, and L. Zhao, Kinetic energy balance in turbulent particle-laden channel flow, Phys. Fluids **32**, 073307 (2020).
[59] G. Wang, H. J. Park, and D. H. Richter, Effect of computational domain size on inertial particle one-point statistics in open channel flow, Int. J. Multiphase Flow **125**, 103195 (2020).

[60] J. Zhou, R. J. Adrian, S. Balachandar, and T. M. Kendall, Mechanisms for generating coherent packets of hairpin vortices in channel flow, J. Fluid Mech. **387**, 353 (1999).
[61] See Supplemental Material at http://link.aps.org/supplemental/10.1103/PhysRevFluids.9.034301 for instantaneous distributions of isosurfaces of $\lambda_2^+ = -0.012$, particles, and streamwise velocity fluctuation.
[62] Q. Wang, K. D. Squires, M. Chen, and J. B. McLaughlin, On the role of the lift force in turbulence simulations of particle deposition, Int. J. Multiphase Flow **23**, 749 (1997).
[63] D. W. Rouson and J. K. Eaton, On the preferential concentration of solid particles in turbulent channel flow, J. Fluid Mech. **428**, 149 (2001).
[64] M. Righetti and G. P. Romano, Particle-fluid interactions in a plane near-wall turbulent flow, J. Fluid Mech. **505**, 93 (2004).
[65] M. Lee and R. D. Moser, Direct numerical simulation of turbulent channel flow up to $\mathrm{Re}_\tau \approx 5200$, J. Fluid Mech. **774**, 395 (2015).
[66] D. H. Richter, Turbulence modification by inertial particles and its influence on the spectral energy budget in planar Couette flow, Phys. Fluids **27**, 063304 (2015).
[67] R. J. Adrian, *Stochastic Estimation of the Structure of Turbulent Fields* (Springer, Berlin, 1996), pp. 145–195.
[68] F. Picano, W. P. Breugem, and L. Brandt, Turbulent channel flow of dense suspensions of neutrally buoyant spheres, J. Fluid Mech. **764**, 463 (2015).
[69] S. Pirozzoli, Searching for the log law in open channel flow, J. Fluid Mech. **971**, A15 (2023).
[70] P. L. Johnson, Predicting the impact of particle-particle collisions on turbophoresis with a reduced number of computational particles, Int. J. Multiphase Flow **124**, 103182 (2020).
[71] M. Caporaloni, F. Tampieri, F. Trombetti, and O. Vittori, Transfer of particles in nonisotropic air turbulence., J. Atmos. Sci. **32**, 565 (1975).
[72] J. B. Mclaughlin, Inertial migration of a small sphere in linear shear flows, J. Fluid Mech. **224**, 261 (1991).
[73] R. Mei, An approximate expression for the shear lift force on a spherical particle at finite Reynolds number, Int. J. Multiphase Flow **18**, 145 (1992).
[74] G. Chen, H. Wang, K. Luo, and J. Fan, Two-way coupled turbulent particle-laden boundary layer combustion over a flat plate, J. Fluid Mech. **948**, A12 (2022).
[75] J. B. McLaughlin, The lift on a small sphere in wall-bounded linear shear flows, J. Fluid Mech. **246**, 249 (1993).
[76] M. Chen and J. B. Mclaughlin, A new correlation for the aerosol deposition rate in vertical ducts, J. Colloid Interface Sci. **169**, 437 (1995).
[77] P. Cherukat and J. B. Mclaughlin, The inertial lift on a rigid sphere in a linear shear flow field near a flat wall, J. Fluid Mech. **263**, 1 (1994).
[78] R. Kurose and S. Komori, Drag and lift forces on a rotating sphere in a linear shear flow, J. Fluid Mech. **384**, 183 (1999).
[79] A. Giusti, F. Lucci, and A. Soldati, Influence of the lift force in direct numerical simulation of upward/downward turbulent channel flow laden with surfactant contaminated microbubbles, Chem. Eng. Sci. **60**, 6176 (2005).
[80] D. Molin, C. Marchioli, and A. Soldati, Turbulence modulation and microbubble dynamics in vertical channel flow, Int. J. Multiphase Flow **42**, 80 (2012).
[81] J. K. Eaton, Two-way coupled turbulence simulations of gas-particle flows using point-particle tracking, Int. J. Multiphase Flow **35**, 792 (2009).
[82] P. Gualtieri, F. Picano, G. Sardina, and C. Casciola, Clustering and turbulence modulation in particle-laden shear flows, J. Fluid Mech. **715**, 134 (2013).
[83] D. H. Richter and P. P. Sullivan, Momentum transfer in a turbulent, particle-laden Couette flow, Phys. Fluids **25**, 053304 (2013).
[84] G. Wang, K. O. Fong, F. Coletti, J. Capecelatro, and D. H. Richter, Inertial particle velocity and distribution in vertical turbulent channel flow: A numerical and experimental comparison, Int. J. Multiphase Flow **120**, 103105 (2019).